Real-time Forecast of Hurricane-induced Damage Risk to Envelope Systems of Engineered Buildings through Metamodeling

Bowei Li[a], Seymour M.J. Spence[a,1,*]

[a]*Department of Civil and Environmental Engineering, University of Michigan, Ann Arbor, MI 48109, USA*

Abstract

The growing intensity and frequency of extreme wind events, together with the continued economic and population growth of coastal areas, has created an urgent need for methodologies that can inform emergency responders and managers of the increasing risk to the infrastructure of these areas. To this end, this work outlines a real-time risk forecast framework for hurricane-induced damage to building envelope systems of engineered buildings. Damage is quantified through a recently introduced multi-demand and coupled progressive fragility model, with a full range of uncertainty in structural properties, capacities, and wind stochasticity. To enable real-time assessment, an efficient Kriging metamodel is introduced to capture the damage statistics conditioned on intensity measures. From official real-time hurricane advisories, site-specific intensity measures are forecast based on a parametric wind field model while considering the uncertainty in, among others, the hurricane track, pressure deficit, and filling model. Damage risk is predicted through propagating uncertainty by Monte Carlo simulation through the Kriging metamodels calibrated to forecast intensity measures. For illustration, the real time damage risk of the envelope system of a 45-story building located in Miami, Fl, was estimated for hurricanes Matthew (2016), Irma (2017), and Dorian (2019). The efficiency and accuracy of proposed is demonstrated.

Keywords: Real Time Risk Forecast, Building Envelope, Hurricane-induced Damage, Uncertainty Propagation, Metamodeling

*Corresponding author

Email addresses: jacklbw@umich.edu (Bowei Li), smjs@umich.edu (Seymour M.J. Spence)

[1]Tel. +1-734-764-8419, Fax +1-734-764-4292

1. Introduction

The growing frequency and intensity of hurricanes is increasing the risk of catastrophic wind-induced damage to coastal areas [1, 2, 3, 4]. This is especially true if it is kept in mind that coastal areas often have significant socioeconomic importance to a region with expanding populations and economies [5]. Within this context, emergency response and management is vital when these areas are subject to upcoming hurricanes [6]. Typically, successful emergency response and management relies on decision-making that requires real time information on the risks and consequences of catastrophic damage and loss from upcoming hurricanes [7, 8]. Within this context, the goal of this research is to develop a real-time forecast framework for estimating the risk of damage to building envelope systems of engineered buildings, e.g., critical facilities, from imminent hurricanes.

Important to this goal are the pioneering efforts devoted to the development of frameworks for estimating the response of residential buildings subject to extreme winds. These include models that enable the estimation of the damage, [9, 10, 11], reliability [12, 13, 14], fragility [15, 16, 17], risk/losses [18, 19, 20, 21, 22, 23], and community level vulnerability [24, 4] of such systems. In addition, the development of modeling frameworks, e.g., HAZUS-MH [25, 26] and the Florida Public Hurricane Loss Model (FPHLM) [27, 28], provide holistic and standardized methodologies for hurricane risk analyses of portfolios of buildings. Motivated by the significant success seen in reducing seismic risk, recent trends in performance assessment of individual buildings subject to extreme winds have focused on the development of frameworks that enable the application of performance-based engineering. This has led to development of numerous methodologies for the analysis of residential buildings [29, 30, 31, 32], high-rise buildings [33, 34, 35, 36, 37, 38, 39, 40], as well as other infrastructure [41, 42]. In general, the performance assessment of these approaches is supported by more a comprehensive and quantitative probability-based procedure [15, 43]. As such, they are very well suited for the performance assessment of engineered systems, e.g., the high-rise buildings considered in this work. Of the performance-based approaches developed to date, those recently introduced in [39, 44, 45] are of particular interest to this work as they enable the explicit damage assessment of the building envelope of engineered system.

A major difficulty in applying these frameworks for real-time damage prediction is the

significant computational effort required for their evaluation. To circumvent this issue, metamodeling techniques, which seek to define a computationally efficient model of the model without loss of accuracy, is an approach with strong potential. Indeed, metamodeling techniques have been gaining immense interest in computationally intensive applications, e.g., uncertainty propagation and optimization. Polynomial regression is among the earliest of these approaches and has been widely used due to its ease in implementation and high efficiency in predictions [46]. Nonetheless, the determination of an appropriate polynomial order is generally not trivial, as an order that is too low will generally lead to low accuracy due to incapability to capture local details, while an excessively high order can lead to overfitting and numerical problems. A candidate solution to this issue is to determine the basis function adaptively, e.g., through subset search [47, 48, 42], multivariate adaptive regression splines (MARS) [49, 50, 51], or adaptive basis function construction (ABFC) [52, 50, 51]. The MARS approach, which can be viewed as a hierarchical forward/backward stepwise subset selection procedure, introduced recursive partitioning while using spline basis, and thus have not only good continuity but also the malleability to capture localized features. The ABFC approach, on the other hand, describes the polynomials through a state matrix while performing searches with heuristic schemes, and therefore avoids the requirement of a predesignated set of basis while also reducing the effort required during the search process. The aforementioned schemes generally assume all known data points are equally important in the prediction at new inquiry points, i.e., in assigning importance, they do not consider the distances from the inquiry point to known data points. To overcome this, the moving least square scheme [53, 54, 7] introduced a distance-related weight therefore emphasizing the contribution to the prediction of the data points closer to the current inquiry point. This adaptiveness is not shared with other popular techniques, e.g., neural networks [55, 56], and enables higher prediction accuracy given the same set of basis functions. A limitation of this scheme is the relatively large computational burden associated with the matrix inversion necessary in making the prediction for each new inquiry point. As an alternative, Kriging-based schemes retain the merit of emphasizing data closer to the inquiry point, while also achieving high computational efficiency by not requiring any intensive operations in making predictions [57, 50, 7, 8, 51]. In addition, this best linear unbiased predictor [58] is interpola-

tive, and therefore exact at the support data points, while also providing a direct estimate of the epistemic uncertainty introduced by the model itself.

In this work, a real-time risk forecast framework for hurricane-induced damage to envelope systems of engineered buildings is introduced. Damage is estimated through a recently introduced high-fidelity multi-demand progressive fragility model that enables probabilistic evaluation of hurricane-induced damage while considering a full range of uncertainties [39, 44] i.e., uncertainties in the hurricane forecasts (track and wind field), wind pressure processes (wind load stochasticity), structural properties in terms of damping, component capacities, and coupling between envelope damage states. To address the computational demand of the high-fidelity damage model, and therefore enable real-time application, a Kriging metamodeling scheme is introduced for describing the mapping from site-specific intensity measures, e.g., wind speeds and directions, to conditional statistics of the envelope damages. For real-time forecast of damage, the metamodel is developed to accept information from parametric wind field models that provide prediction of the site specific intensity measures from typical information provided by hurricane advisories issued by the national hurricane center (NHC). Uncertainty in forecasting the site specific intensity measures is considered through introducing uncertainty in the predicted hurricane tracks, pressure deficit, and filling model. Monte Carlo simulation is used to propagate uncertainty through the metemodels and therefore provide estimates of the risk of wind-induced damage to the building envelope. To illustrate the framework, the real time prediction of damage risk to the envelope system of a 45-story building located in Miami, Florida, and subject to three historical hurricane scenarios is considered. The calibrated metamodel is seem to maintain high accuracy while being over four orders of magnitude faster than the high-fidelity model therefore successfully enabling real time damage risk forecast.

2. Real-time forecast of site-specific wind intensity

2.1. Preamble

This section outlines a scheme for forecasting site-specific wind intensity based on the parametric wind field models outlined in [59], as well as information from official hurricane advisory streams, e.g., those from the national hurricane center of the United States. In

particular, for an imminent hurricane, information from the advisories on hurricane track and intensity is used as input to the parametric wind field model therefore enabling forecast of the site-specific wind intensity measures, e.g., the maximum site specific wind speed and associated direction to occur over the evolution of the imminent hurricane. As outlined in [60], this site specific information on the hurricane intensity can be used to provide high-fidelity probabilistic estimates of envelope damage to engineered buildings.

2.2. Hurricane forecast

Hurricane forecasting has experienced significant advances over the past several decades. The NHC, for example, provides forecast/advisory for all Atlantic, eastern Pacific, and central Pacific tropical and subtropical regions [61]. The forecast/advisory for each hurricane contains, among other information: the current watches and warnings; the track forecast, defined by the latitude, $\bar{\phi}_{t_\mathrm{T}}$, and longitude, $\bar{\lambda}_{t_\mathrm{T}}$, of the center of the hurricane at $t_\mathrm{T} = 0$ (present), 12, 24, 36, 48, 72, 96, and 120 hours into the future; and current intensity expressed as the central pressure p_0. This information is usually released every six hours at 03:00, 09:00, 15:00, and 21:00 UTC. In addition, the NHC verifies the forecasts against the hurricane's "best track" database by NHC's post-storm analyses, and provides the associated error data for the period 1970 to the present [62].

Based on the aforementioned information, stochastic hurricane track samples (ϕ_{t_T}, λ_{t_T}) can be generated, as shown in Figure 1, by adding to the track forecast coordinates ($\bar{\phi}_{t_\mathrm{T}}$, $\bar{\lambda}_{t_\mathrm{T}}$) random errors ($e_{\phi,t_\mathrm{T}}$, e_{λ,t_T}):

$$(\phi_{t_\mathrm{T}}, \lambda_{t_\mathrm{T}}) = (\bar{\phi}_{t_\mathrm{T}}, \bar{\lambda}_{t_\mathrm{T}}) + (e_{\phi,t_\mathrm{T}}, e_{\lambda,t_\mathrm{T}}) \tag{1}$$

In particular, the statistical properties of the errors (e_{ϕ,t_T}, e_{λ,t_T}) are expected to be consistent with the official error database. To this end, along- and cross-track forecast errors ($e_{\mathrm{A},t_\mathrm{T}}$, $e_{\mathrm{C},t_\mathrm{T}}$) are assumed to follow a multivariate Gaussian distribution:

$$[e_{\mathrm{A},0}, e_{\mathrm{C},0}, e_{\mathrm{A},12}, e_{\mathrm{C},12}, ...] \sim \mathcal{N}([\bar{e}_{\mathrm{A},0}, \bar{e}_{\mathrm{C},0}, \bar{e}_{\mathrm{A},12}, \bar{e}_{\mathrm{C},12}, ...], \mathbf{\Sigma}_e) \tag{2}$$

where the mean error vector $[\bar{e}_{\mathrm{A},0}, \bar{e}_{\mathrm{C},0}, \bar{e}_{\mathrm{A},12}, \bar{e}_{\mathrm{C},12}, ...]$ and covariance matrix $\mathbf{\Sigma}_e$ are calculated from the forecast error database of the last five years after official NHC verification [62]. Subsequently, error samples ($e_{\mathrm{A},t_\mathrm{T}}$, $e_{\mathrm{C},t_\mathrm{T}}$) at all t_T can be generated from Eq. (2), transformed

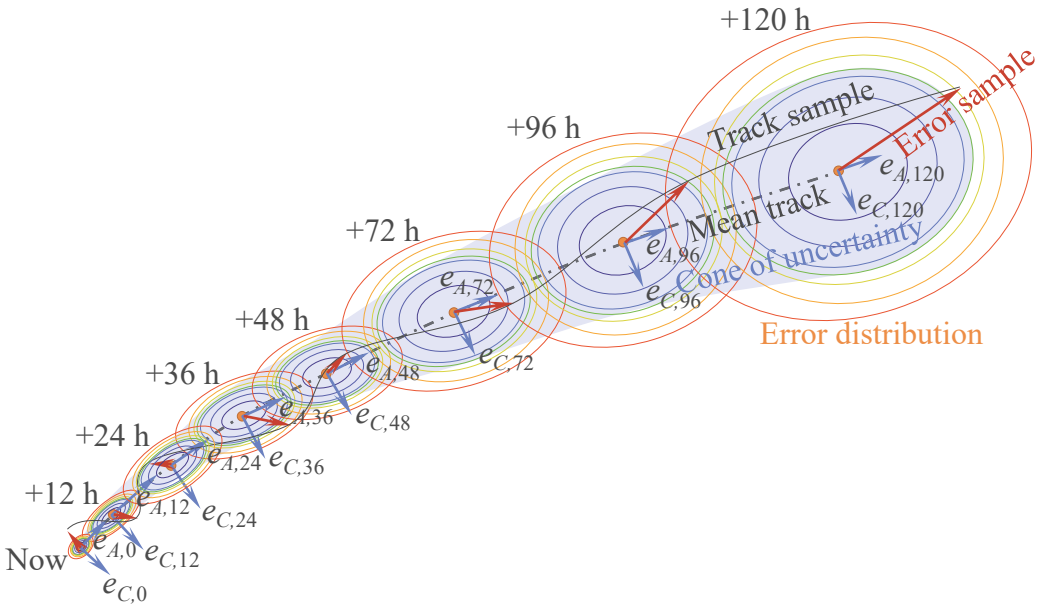

Figure 1: Real-time track forecast and generation of track samples.

to the geographic coordinate system as longitude $e_{\phi,t_{\mathrm{T}}}$ and latitude $e_{\lambda,t_{\mathrm{T}}}$, and added to the original prediction $(\bar{\phi}_{t_{\mathrm{T}}},\ \bar{\lambda}_{t_{\mathrm{T}}})$ therefore defining the track samples of Eq. (1). In addition, techniques such as cubic spline interpolation can be implemented to infer hurricane positions between any two consecutive predicted times.

2.3. Wind field model

At each time instant of a track sample, to evaluate the site-specific wind intensity, a parametric hurricane wind field model is implemented [59]. This model takes the current central pressure deficit Δp_0 (the difference between the standard air pressure and the current central pressure p_0) and the radius of the maximum wind, r_M, as parameters, and gives both the tangential and radial velocity components at 500 m above the sea level as:

$$\mathbf{v}(r,\beta;t) = v_{\mathrm{M}}\left[\sqrt{r'^{-B}\exp(1-r'^{-B})+a^2r'^2}-ar'\right](\mathbf{e}\sin\beta-\mathbf{n}\cos\beta),\ r'=\frac{r}{r_M},\ a=\frac{fr_{\mathrm{M}}}{2v_{\mathrm{M}}} \tag{3}$$

$$\mathbf{u}(r,\beta;t) = \left[\frac{\frac{K}{r}\frac{\partial}{\partial r}\left(r\frac{\partial v}{\partial r}\right)-K\frac{v}{r^2}-\frac{C_d v^2}{h}\sqrt{1+\alpha_M^2}}{\frac{\partial v}{\partial r}+\frac{v}{r}+f}\right](\mathbf{e}\cos\beta-\mathbf{n}\sin\beta),\ v=||\mathbf{v}|| \tag{4}$$

where $\mathbf{v}(r,\beta;t)$ and $\mathbf{u}(r,\beta;t)$ are respectively the tangential and radial velocity fields in the polar coordinate system $(r,\ \beta)$ with origin at the hurricane center; B is the Holland number

that defines the air pressure distribution; K is the diffusion coefficient; f is the Coriolis parameter, evaluated as $f = 2\Omega \sin \phi_t$, with $\Omega \sim 7.2921 \times 10^{-5}$ rad/s the rotation rate of the Earth and ϕ_t the latitude of the hurricane center; $C_d \sim 0.0015$ is the drag coefficient related to the boundary layer averaged velocity; h is the boundary layer thickness; $\alpha_M = -\frac{||\mathbf{u}||}{||\mathbf{v}||}$ is the deflection coefficient that can be assumed to be constant [63, 64]; v_M is the maximum wind field velocity than can be estimated as:

$$v_M = \sqrt{\frac{B\Delta p(t)}{e\rho_a(1+\alpha_M^2)}} \tag{5}$$

where e is Euler's number; $\rho_{\mathrm{a}} \sim 1.15$ kg/m^3 is the air density; $\Delta p(t)$ is the center pressure deficit (with $\Delta p(0) = \Delta p_0$), which can be estimated through the filling-rate model [65]:

$$\Delta p(t) = \Delta p(t_{\mathrm{l}}) \exp\left[-a_{\mathrm{f}}(t - t_{\mathrm{l}})\right] \tag{6}$$

where t_{l} is the time instant when the hurricane makes landfall; a_f is the filling constant, with the uncertainty considered through a zero mean Gaussian variable ϵ:

$$a_{\mathrm{f}} = a_{\mathrm{f},0} + a_{\mathrm{f},1}\Delta p_0 + \epsilon \tag{7}$$

where $a_{\mathrm{f},0}$ and $a_{\mathrm{f},1}$ are region-specific coefficients available in Vickery and Twisdale [65]. The filling model simulates the decay process of the hurricane intensity after making landfall due to the increase of its central pressure, i.e., the "filling" of the pressure deficit.

By superimposing the translation speed of the hurricane with the tangential and radial velocity components relative to the hurricane center, the resultant wind speed field, i.e., relative to the ground, is given by:

$$\mathbf{v}_{\mathrm{s}}(r, \beta; t) = \mathbf{v}(r, \beta; t) + \mathbf{u}(r, \beta; t) + \mathbf{c}\exp(-\frac{r}{r_{\mathrm{G}}}) \tag{8}$$

where $\mathbf{c}$ is the translation speed vector of the hurricane while r_{G} is the environmental length scale that governing the radial decay of $\mathbf{c}$.

Based on Eq. (8), the site-specific hourly-mean wind speed $\tilde{v}_H(t)$ can be obtained through:

$$\tilde{v}_H(t) = 0.68 \cdot \left(\frac{z_0}{z_{01}}\right)^{\delta} \frac{\ln\left[H/z_0\right]}{\ln\left[H_{\mathrm{met}}/z_{01}\right]} ||\mathbf{v}_{\mathrm{s}}(r_{\mathrm{s}}, \beta_{\mathrm{s}}; t)|| \tag{9}$$

where $(r_{\mathrm{s}}, \beta_{\mathrm{s}})$ are the polar coordinates locating the building site of interest with respect to the hurricane eye; z_0 and z_{01} are respectively the roughness length at the building site and

meteorological site; H and H_{met} (typically 10 m) are the height at the top of the building and the meteorological site reference height, respectively; δ is an empirical constant; 0.68 is dimensionless coefficient used for converting the wind speeds at the height of 500 m to the meteorological reference height, H_{met}, in open terrain [66, 65, 67]. The associated wind direction, $\tilde{\alpha}(t) \in [0°,\ 360°)$, defined as the angle between $\mathbf{v}_{\text{s}}(||\mathbf{r}_{\text{sc}}||, \beta; t)$ and $\mathbf{n}$, can also be obtained. The site-specific wind intensity measures, namely the site-specific maximum wind speed, $v_H = \tilde{v}_H(\hat{t}) = \max|\tilde{v}_H(t)|$, and associated direction $\alpha = \tilde{\alpha}(\hat{t})$, can be subsequently estimated.

Through Monte Carlo simulation, the aforementioned forecast model can be used to provide samples of the the site-specific wind intensity measures (v_H, α) with full consideration of the uncertainty inherent to hurricane forecast (e.g., track stochasticity and central pressure deficit) and adopted models (e.g., the radius of the maximum wind and filling rate). Moreover, this framework is computationally treatable, allowing for the rapid generation of a large number of samples of (v_H, α) in real-time.

3. High-fidelity building envelope damage assessment model

To evaluate hurricane-induced damage to envelope systems of engineered buildings, the coupled multi-demand progressive damage assessment framework outlined in Ouyang and Spence [39, 44] is adopted. This high-fidelity assessment framework allows for the consideration of the coupled and time-evolving nature of damages induced by different wind demands.

3.1. Data-informed stochastic wind pressure

The estimation of damage to building envelopes for a given realization of the intensity measures, i.e. a realization of the the pair (v_H, α), requires the modeling of the external dynamic wind pressures. These can be seen to represent realizations of stationary multivariate non-Gaussian stochastic processes. As outlined in [44], the generation of realizations of this stochastic process can be informed by building specific wind tunnel test data in the form of time-varying vectors of external dynamic pressure coefficients, $\mathbf{C}_{p,\text{e}}(\alpha; t)$, measured at a series of carefully located taps on the surface of a rigid scale model of the building for a series of discrete wind directions $\alpha \in \{\alpha_1, \alpha_2, ...\}$. After appropriate scaling to a wind speed of

interest through standard Strouhal number matching [68], this data can be used to calibrate a Gaussian representation of the external pressure coefficients with the expected turbulence levels and complex aerodynamics seen in the wind tunnel (e.g., vortex shedding and detached flow) being captured. Data-driven translation models can then be used to capture any non-Gaussian features.

The Gaussian process, $\mathbf{C}_{p,\mathrm{e}}^{\mathcal{GP}}(t;\alpha)$, is defined from the estimation of the second order statistical properties, i.e., the mean $\bar{\mathbf{C}}_{p,\mathrm{e}}(t;\alpha)$ and cross power spectral density matrix $\mathbf{\Sigma}_{\mathbf{C}_{p,\mathrm{e}}}(\omega;\alpha)$, of the measured wind tunnel data. Subsequently, a proper orthogonal decomposition (POD)-based reduction of $\mathbf{\Sigma}_{\mathbf{P}_{p,\mathrm{e}}}(\omega;\alpha)$ is performed for each wind direction, α, and discrete frequency point, ω, by solving the following eigenvalue problem [69]:

$$\mathbf{\Sigma}_{\mathbf{C}_{p,\mathrm{e}}}(\omega;\alpha)\mathbf{\Psi}_i(\omega;\alpha) = \Lambda_i(\omega;\alpha)\mathbf{\Psi}_i(\omega;\alpha) \tag{10}$$

where $\mathbf{\Psi}_i(\omega;\alpha)$ and $\Lambda_i(\omega;\alpha)$ are respectively the ith spectral POD mode shape and eigenvalue of $\mathbf{\Sigma}_{\mathbf{C}_{p,\mathrm{e}}}$. Typically, as the energy of the signal is generally associated with a few lower-order POD modes, the Gaussian process can thus be well-approximated from the first $m_{p,\mathrm{e}}$ subprocesses, as:

$$\mathbf{C}_{p,\mathrm{e}}^{\mathcal{GP}}(t;\alpha) \approx \hat{\mathbf{C}}_{p,\mathrm{e}}^{\mathcal{GP}}(t;\alpha) = \bar{\mathbf{C}}_{p,\mathrm{e}}(t;\alpha) + \sum_{i=1}^{m_{p,\mathrm{e}}} \mathbf{C}_{p,\mathrm{e}}^{\mathcal{GP}_i}(t;\alpha) \tag{11}$$

where $\mathbf{C}_{p,\mathrm{e}}^{\mathcal{GP}_i}(t;\alpha)$ is the ith independent subprocess generated for the ith POD mode $\mathbf{\Psi}_i(\omega;\alpha)$ and eigenvalue $\Lambda_i(\omega;\alpha)$ as:

$$\mathbf{C}_{p,\mathrm{e}}^{\mathcal{GP}_i}(t;\alpha) = \sum_{j=0}^{n_\omega-1} 2|\mathbf{\Psi}_i(\omega_j;\alpha)|\sqrt{\Lambda_i(\omega_j;\alpha)\Delta\omega}\cos\left(\omega_j t + \boldsymbol{\theta}_j(\omega_j) + \theta_{ij}\right) \tag{12}$$

where $\omega_j = j\Delta\omega$ is the jth frequency point with n_ω the total number of frequency points and $\Delta\omega$ the frequency step size, θ_{ij} is a random phase angles uniformly distributed in $[0, 2\pi]$, while $\boldsymbol{\theta}_j(\omega_j)$ is given by:

$$\boldsymbol{\theta}_j(\omega_j) = \arctan\left[\frac{\mathrm{Im}(\mathbf{\Psi}_i(\omega_j;\alpha))}{\mathrm{Re}(\mathbf{\Psi}_i(\omega_j;\alpha))}\right] \tag{13}$$

The non-Gaussian features of the pressure coefficients can be effectively introduced by transforming the marginal Gaussian distributions of $\hat{\mathbf{C}}_{p,\mathrm{e}}^{\mathcal{GP}}(t;\alpha)$ to non-Gaussian marginal distributions using translation models [70], therefore defining a stationary and multivariate

non-Gaussian representation of the external pressure coefficients $\mathbf{C}_{p,\mathrm{e}}(t;\alpha)$. In particular, the element-wise translation models capturing the non-Gaussian features are calibrated once again to the building specific wind tunnel test data. To this end, kernel-Pareto mixture models are adopted in which the raw wind tunnel data is partitioned into into a lower tail region, a central region, and an upper tail region. Kernel density is then used to represent the distribution of the data of the central region, while extreme Pareto distributions are considered for the tail regions [71]. Once $\mathbf{C}_{p,\mathrm{e}}(t;\alpha)$ is generated, the external dynamic pressure coefficient at an arbitrary location $\boldsymbol{\xi}$, i.e., a point outside of where pressures were measured on the building model used in the wind tunnel tests, can be obtained through instantaneous interpolation of $\mathbf{C}_{p,\mathrm{e}}(t;\alpha)$, therefore defining $\mathbf{C}_{p,\mathrm{e}}(t;\alpha,\boldsymbol{\xi})$.

3.2. Wind demands

The demands of the envelope damage assessment framework are the in-plane deformations of the envelope components due to the interstory drift response of the structural system, as well as the out-of-plane net pressure on the envelope components. To evaluate the interstory drifts, the structural responses of the system is estimated by solving the following equation of motion:

$$\mathbf{M}\ddot{\mathbf{U}}(t) + \mathbf{C}\dot{\mathbf{U}}(t) + \mathbf{K}\mathbf{U}(t) = \mathbf{F}(t; v_H, \alpha) \tag{14}$$

where $\ddot{\mathbf{U}}(t)$, $\dot{\mathbf{U}}(t)$, and $\mathbf{U}(t)$ are respectively the acceleration, velocity, and displacement response vectors; $\mathbf{M}$, $\mathbf{C}$, and $\mathbf{K}$ are respectively the mass, damping, and stiffness matrices of the structural system; and $\mathbf{F}(t; v_H, \alpha)$ are the stochastic wind loads obtained through the integration of the external wind pressures derived from the external pressure coefficients of Section 3.1 as:

$$\mathbf{p}_e(t; v_H, \alpha, \boldsymbol{\xi}) = \frac{1}{2}\rho_{\mathrm{a}} v_H^2 \mathbf{C}_{p,\mathrm{e}}(t; \alpha, \boldsymbol{\xi}) \tag{15}$$

where ρ_{a} is the density of air. It should be noted while Eq. (14) is written as a linear elastic system, this assumption is by no means central to the framework of this work that can be equally applied to general nonlinear systems. From $\mathbf{U}(t)$, the interstory drift ratios, $Dr(t)$, at any location, $\boldsymbol{\xi}$, of the building envelope can be directly estimated. Due to the progressive and coupled nature of wind-induced damage to building envelopes, the entire time history

of interstory response, $Dr(t)$, must be considered as the engineering demand parameter (as opposed to the peak value commonly adopted in seismic damage modeling).

The out of plane net pressure demand acting on an envelope component of location $\boldsymbol{\xi}$ is defined as the difference between the external and the internal pressure and therefore as:

$$p_{\mathrm{n}}(t; v_H, \alpha, \boldsymbol{\xi}) = \frac{1}{2}\rho_{\mathrm{a}} v_H^2 \left[C_{p,\mathrm{e}}(t; \alpha, \boldsymbol{\xi}) - C_{p,\mathrm{i}}(t; \boldsymbol{\xi})\right] \tag{16}$$

where $C_{p,\mathrm{i}}(t, \boldsymbol{\xi})$ is the internal dynamic pressure coefficient at the envelope element, obtained as outlined in [39]. In particular, in evaluating $P_{p,\mathrm{i}}(\boldsymbol{\xi}; t)$, the building system is considered as a set of interconnected air spaces with both internal/external openings. The external openings are those in the building envelope. In general, at the beginning of a hurricane the building is considered enclosed, i.e., no external openings exist. As damage occurs, external openings will appear. As discussed in [39], this not only significantly changes the internal pressure stochastic process but also couples the drift and pressure demands as external openings generated by drift will in general effect the net pressure demand. Once external openings occur, the internal dynamic pressure coefficient, $C_{p,\mathrm{i}}(t, \boldsymbol{\xi})$, can be estimated from solving the unsteady-isentropic Bernoulli equation of transient airflow at each opening [72, 73] through an explicit 4th order Runge-Kutta method. It should be noted that envelope components will in general experience static fatigue/delayed failure, which, instead of being related to instantaneous pressure, $p_{\mathrm{n}}(t; \boldsymbol{\xi})$, are better related to equivalent net pressure [74]:

$$p_{\mathrm{eq}}(t; v_H, \alpha, \boldsymbol{\xi}) = \left(\frac{1}{t_{\mathrm{eq}}} \int_0^t \left[p_n(t; v_H, \alpha, \boldsymbol{\xi})\right]^s\right)^{\frac{1}{s}} \tag{17}$$

where t_{eq} is the reference duration, typically taken between 3 s to 60 s and s is an empirical exponent.

3.3. Envelope capacities and damage measures

The susceptibility of each envelope component of the building system to damage induced by excessive net pressure, $p_{\mathrm{eq}}(t; v_H, \alpha, \boldsymbol{\xi})$, and/or dynamic drift, $Dr(t; v_H, \alpha, \boldsymbol{\xi})$, demands, is modeled through considering suites of N_p pressure-induced damage states $\{\mathrm{DS}_i^p : \ i = 1, \ 2, ..., \ N_p\}$ and N_{Dr} drift-induced damage states $\{\mathrm{DS}_i^{Dr} : \ i = 1, \ 2, ..., \ N_{Dr}\}$. Each suite of damage states are considered to follow a sequential damage logic, i.e., the occurrence of

a certain damage state implies that all preceding damage states have occurred. Each suite of damage states is associated with a suite of sequential thresholds, i.e., capacities of the form $\{C_i^{Dr} : \ i = 1, \ 2, ..., \ N_{Dr}, \ C_{i-1}^{Dr} \leq C_i^{Dr}\}$ and $\{C_i^{p} : \ i = 1, \ 2, ..., \ N_{p}, \ C_{i-1}^{p} \leq C_i^{p}\}$. In particular, in defining the capacity of an envelope component to resist net pressure, the common assumption of a parallel mechanism is assumed, i.e., for an envelope component with two panes of glass, it is assumed that each glass pane resists 50% of p_{eq} [75]. The exceedance at any point during the evolution of a hurricane of a threshold by the respective pressure or drift demand, i.e., $p_{\text{eq}}(t;\boldsymbol{\xi})$ or $Dr(t;\boldsymbol{\xi})$, indicates the occurrence of the damage state. Uncertainty in the capacities is modeled through suites of sequential fragility functions (one fragility function or each damage state). In practice, for a given time instant $\hat{t} \in [0, T]$ with T the duration of the event, the current damage states, $\mathbf{DS}(\hat{t})$, of an envelope component are the damage states associated with the highest capacities to have been exceeded in $[0, \hat{t}]$ for each of the groups. In addition, it should be noted that the drift and pressure induced damage states will in general be coupled, as, for instance, cracks induced by excessive drift deformation will generally reduce the capacity of the envelope components to resist net pressure and viceversa. To account for this coupling, a reduction factor, $\rho_C(\mathbf{DS})$, for the capacities is generally considered. Initially $\rho_C(\mathbf{DS}) = 1$ and will degrade upon the occurrence of a coupled damage state. This coupling, together with the coupling between the demands discussed in Section 3.2, makes the process of damage accumulation progress in nature and requires the simulation of the damage process over the entire duration, T, of the wind event.

3.4. High fidelity probabilistic envelope performance evaluation

As outlined in [39, 44, 45, 60], by embedding the models of Sections 3.1 to 3.3 in general uncertainty propagation frameworks (e.g., Monte Carlo simulation schemes and their derivatives), high-fidelity estimates of the probabilistic performance of the envelope system of engineered buildings subject to extreme winds can be obtained. In particular, the generality of the models enable a full range of uncertainty/stochasticity in, for example, the structural properties (e.g., $\mathbf{M}$, $\mathbf{C}$, and $\mathbf{K}$), the wind excitation (e.g., $C_{p,\text{e}}(t;\alpha,\boldsymbol{\xi})$), the envelope capacities through the fragility functions of the damage thresholds, and damage coupling through $\rho_C(\mathbf{DS})$, to be included. The computational burden of this high-fidelity approach to probabilistic performance estimation of envelope systems is significant as it requires time

stepping through the entire hurricane event of duration T and solving at each time step the models of Sections 3.1 to 3.3. This includes simulating external stochastic wind pressures, solving nonlinear internal pressure models (multiple times if cascading failure occurs), integrating the dynamic equations of motions of the structural system, and performing the coupled damage analysis of Section 3.3 for each damageable component of the envelope system (typically in the order of thousands). Notwithstanding how in [60] it was shown that for accurate estimation of envelope damage, the simulation need only be carried for the pair (v_H, α) with $T = 1$ hour, typical run times on powerful multi-core desktop machines are in the order of days therefore precluding real-time damage predication.

4. Metamodeling

4.1. Damage measures

As discussed in Section 3.4, the high-fidelity assessment framework is computationally prohibitive for application in real-time damage assessment. To circumvent this issue, this work is focused on developing a metamodel of the assessment framework that is capable of providing equally comprehensive information on the damage to the envelope system while requiring a fraction of the computational effort. To facilitate metamodeling, it is convenient to introduce, without any loss of generality, the following dimensionless damage measure for each damage state of each damageable envelope component:

$$D_C = \frac{\min_{t\in[0,T]} \left[\rho_C(\mathbf{DS})C - edp(t)\right]}{\bar{C}} \tag{18}$$

where C is the initial capacity of the envelope component to one of its potential damage states while $\bar{C}$ is the expected capacity. In particular, D_C is a strictly decreasing function over the duration of the wind event with $D_C < 0$ indicating damage and $\mathbb{E}[D_C] = 1$ prior to any damage and in absence of demand. Given specific values of the intensity measures, (v_H, α), the uncertainty/stochasticity considered in the damage assessment framework leads to randomness associated with D_C which, in general, can be expressed through the probability density function $p(D_C|v_H, \alpha)$. In this research, the first two moment of the $p(D_C|v_H, \alpha)$, namely the conditional mean $\mu_{D_C|v_H,\alpha}$ and standard deviation $\sigma_{D_C|v_H,\alpha}$, are of interest for characterizing

$p(D_C|v_H, \alpha)$. In the next section, Kriging metamodels will be introduced for approximating $\mu_{D_C|v_H,\alpha}$ and $\sigma_{D_C|v_H,\alpha}$ for each damage state of all envelope components composing the system. It should be noted that this does not exclude the possibility of implementing this framework with different measures for representing $p(D_C|v_H, \alpha)$, e.g., higher-order statistic or kernel smoothing.

4.2. The Kriging metamodel

To address the computational bottleneck of the high-fidelity assessment framework, a Kriging metamodel will be introduced. As in any metamodeling technique, Kriging seeks to establish a computationally efficient surrogate mapping from the space of the inputs $\mathbf{x}$, i.e., the wind intensity measures (v_H, α) in this case, to the space of the output y, i.e., the conditional statistics $\mu_{D_C|v_H,\alpha}$ and $\sigma_{D_C|v_H,\alpha}$ for each damage state of each envelope component of the system. In particular, Kriging is based on the prior assumption that y is a Gaussian process over the space of $\mathbf{x}$:

$$\hat{y}(\mathbf{x}) = \mathbf{g}^{\mathrm{T}}(\mathbf{x})\mathbf{a} + \epsilon_{\mathbf{x}} \tag{19}$$

where $\mathbf{g}(\mathbf{x})$ is a vector of basis functions, with coefficients $\mathbf{a}$ to be calibrated; $\epsilon_{\mathbf{x}}$ is a zero-mean Gaussian process with its autocovariance $\sigma_y^2 R(\mathbf{x}, \mathbf{x}', \boldsymbol{\theta})$ characterized by the parameters collected in $\boldsymbol{\theta}$.

Given a set of observations $\mathbf{S} = \{(\mathbf{x}_i,\ y_i),\ i = 1, 2, ..., n_{\mathbf{x}}\}$, the joint distribution between $\mathbf{S}$ and any new data points, e.g., $\mathbf{S}' = \{(\mathbf{x}'_i,\ y'_i),\ i = 1, 2, ..., n'_{\mathbf{x}}\}$, can be written as:

$$\begin{bmatrix} \mathbf{Y} \\ \mathbf{Y}' \end{bmatrix} \sim \mathcal{N}\left(\begin{bmatrix} \mathbf{G}^{\mathrm{T}} \\ \mathbf{G}'^{\mathrm{T}} \end{bmatrix} \mathbf{a}, \begin{bmatrix} \boldsymbol{R}_{\mathbf{YY}} & \boldsymbol{R}_{\mathbf{YY}'} \\ \boldsymbol{R}^{\mathrm{T}}_{\mathbf{YY}'} & \boldsymbol{R}_{\mathbf{Y}'\mathbf{Y}'} \end{bmatrix} \sigma_y^2 \right) \tag{20}$$

where $\mathbf{Y} = [y_1, \ldots, y_{n_{\mathbf{x}}}]^{\mathrm{T}}$, $\mathbf{Y}' = [y'_1, \ldots, y'_{n'_{\mathbf{x}}}]^{\mathrm{T}}$, $\mathbf{G} = [\mathbf{g}(\mathbf{x}_1), \ldots, \mathbf{g}(\mathbf{x}_{n_{\mathbf{x}}})]$, $\mathbf{G}' = [\mathbf{g}(\mathbf{x}'_1), \ldots, \mathbf{g}(\mathbf{x}'_{n'_{\mathbf{x}}})]$, while $\boldsymbol{R}_{\mathbf{YY}}$ is given by:

$$\boldsymbol{R}_{\mathbf{YY}} = \begin{bmatrix} R(\mathbf{x}_1, \mathbf{x}_1, \boldsymbol{\theta}) & \ldots & R(\mathbf{x}_1, \mathbf{x}_{n_{\mathbf{x}}}, \boldsymbol{\theta}) \\ \vdots & \ddots & \vdots \\ R(\mathbf{x}_{n_{\mathbf{x}}}, \mathbf{x}_1, \boldsymbol{\theta}) & \ldots & R(\mathbf{x}_{n_{\mathbf{x}}}, \mathbf{x}_{n_{\mathbf{x}}}, \boldsymbol{\theta}) \end{bmatrix} \tag{21}$$

with $\boldsymbol{R}_{\mathbf{YY}'}$ and $\boldsymbol{R}_{\mathbf{Y}'\mathbf{Y}'}$ defined similarly when considering $R(\mathbf{x}, \mathbf{x}', \boldsymbol{\theta})$ and $R(\mathbf{x}', \mathbf{x}', \boldsymbol{\theta})$.

The predictive distribution at new points given the known observations $\mathbf{S}$ can therefore be derived as [76]:

$$\mathbf{Y}'|\mathbf{Y} \sim \mathcal{N}\left(\boldsymbol{\mu}_{\mathbf{Y}'|\mathbf{Y}}, \boldsymbol{\Sigma}_{\mathbf{Y}'|\mathbf{Y}}\right) \tag{22}$$

where $\boldsymbol{\mu}_{\mathbf{Y}'|\mathbf{Y}} = \mathbf{G}'^{\mathrm{T}}\mathbf{a} + \boldsymbol{R}_{\mathbf{Y}\mathbf{Y}'}^{\mathrm{T}}\boldsymbol{R}_{\mathbf{Y}\mathbf{Y}}^{-1}(\mathbf{Y} - \mathbf{G}^{\mathrm{T}}\mathbf{a})$ and $\boldsymbol{\Sigma}_{\mathbf{Y}'|\mathbf{Y}} = \boldsymbol{R}_{\mathbf{Y}'\mathbf{Y}'}\sigma_y^2 - \boldsymbol{R}_{\mathbf{Y}\mathbf{Y}'}^{\mathrm{T}}\boldsymbol{R}_{\mathbf{Y}\mathbf{Y}}^{-1}\boldsymbol{R}_{\mathbf{Y}\mathbf{Y}'}\sigma_y^2$ are respectively the mean and covariance of $\mathbf{Y}'$ conditioned on $\mathbf{Y}$. The Kriging predictor is exactly the mean function in Eq. (22). For instance, the Kriging predictor for only a single new point $\hat{y}(\mathbf{x})$ is given by:

$$\hat{y}(\mathbf{x}) = \mathbf{g}^{\mathrm{T}}(\mathbf{x})\mathbf{a} + \mathbf{r}^{\mathrm{T}}(\mathbf{x})\mathbf{b} \tag{23}$$

where $\mathbf{r}(\mathbf{x}) = \boldsymbol{R}_{\mathbf{Y}\hat{y}} = [R(\mathbf{x}_1, \mathbf{x}, \boldsymbol{\theta}) \dots R(\mathbf{x}_{n_\mathbf{x}}, \mathbf{x}, \boldsymbol{\theta})]^{\mathrm{T}}$ and $\mathbf{b} = \boldsymbol{R}_{\mathbf{Y}\mathbf{Y}}^{-1}(\mathbf{Y} - \mathbf{G}^{\mathrm{T}}\mathbf{a})$.

Overall, the predictive distribution contains unknown parameters $\mathbf{a}$ ($\mathbf{b}$ fully depends on $\mathbf{a}$), σ_y^2 and $\boldsymbol{\theta}$, which can be estimated by the maximum likelihood method [77]. In particular, the likelihood function L is defined as:

$$\begin{aligned} L(\mathbf{a}, \sigma_y^2, \boldsymbol{\theta}) &= \ln p(\mathbf{Y}|\mathbf{a}, \sigma_y^2, \boldsymbol{\theta}, \mathbf{x}_1, ..., \mathbf{x}_{n_\mathbf{x}}) \\ &= -\frac{n_\mathbf{x} \ln 2\pi}{2} - \frac{\ln|\boldsymbol{R}_{\mathbf{Y}\mathbf{Y}}|}{2} - \frac{n_\mathbf{x} \ln \sigma_y^2}{2} - \frac{\left(\mathbf{Y} - \mathbf{G}^{\mathrm{T}}\mathbf{a}\right)^{\mathrm{T}} \boldsymbol{R}_{\mathbf{Y}\mathbf{Y}}^{-1} \left(\mathbf{Y} - \mathbf{G}^{\mathrm{T}}\mathbf{a}\right)}{2\sigma_y^2} \end{aligned} \tag{24}$$

The maximum likelihood estimate of $\mathbf{a}$ can be obtained by imposing $\frac{\partial L}{\partial \mathbf{a}} = \mathbf{0}$, therefore giving:

$$\hat{\mathbf{a}} = \left(\mathbf{G}\boldsymbol{R}_{\mathbf{Y}\mathbf{Y}}^{-1}\mathbf{G}^{\mathrm{T}}\right)^{-1} \mathbf{G}\boldsymbol{R}_{\mathbf{Y}\mathbf{Y}}^{-1}\mathbf{Y} \tag{25}$$

Similarly, σ_y^2 can be inferred by imposing $\frac{\partial L}{\partial(\sigma_y^2)} = 0$ which yields:

$$\hat{\sigma}_y^2 = \frac{\left(\mathbf{Y} - \mathbf{G}^{\mathrm{T}}\hat{\mathbf{a}}\right)^{\mathrm{T}} \boldsymbol{R}_{\mathbf{Y}\mathbf{Y}}^{-1} \left(\mathbf{Y} - \mathbf{G}^{\mathrm{T}}\hat{\mathbf{a}}\right)}{n_\mathbf{x}} \tag{26}$$

Unlike $\mathbf{a}$ and σ_y^2, the parameter vector $\boldsymbol{\theta}$ depends on the generally nonlinear function $R(\mathbf{x}, \mathbf{x}', \boldsymbol{\theta})$. Therefore, numerical optimization is generally required for its estimation. This optimization problem can be simplified by substituting Eqs. (25) and (26) into Eq. (24), therefore yielding:

$$\hat{\boldsymbol{\theta}} = \arg\min_{\boldsymbol{\theta}} \left[\ln|\boldsymbol{R}_{\mathbf{Y}\mathbf{Y}}| + n_\mathbf{x} \ln \hat{\sigma}_y^2\right] \tag{27}$$

In Eq. (23), the first term $\mathbf{g}^{\mathrm{T}}(\mathbf{x})\mathbf{a}$ in $\hat{y}(\mathbf{x})$ is essentially a regression model with basis functions collected in $\mathbf{g}(\mathbf{x})$. This term captures the global trend within the observations $\mathbf{S}$. The second term $\mathbf{r}^{\mathrm{T}}(\mathbf{x})\mathbf{b}$, on the other hand, acts as an interpolation model defined through

the radial bases in $\mathbf{r}(\mathbf{x})$, which enables $\hat{y}(\mathbf{x})$ to learn local behaviors in $\mathbf{S}$, in addition to the global trend captured by the regression model. Moreover, $\mathbf{r}(\mathbf{x})$ can be viewed as a weighting function that gives higher weights to observations that are closer to the point $\mathbf{x}$, indicated as $\hat{y}(\mathbf{x})$, with adaptiveness as in the moving least squares approach [7]. In addition, Eq. (23) is highly efficient since all time-consuming calculations, e.g., matrix inversions and numerical optimizations involved in Eqs. (25) to (27), will only need to be performed once for the training set $\mathbf{S}$. This is an important advantage over, for instance, the moving least squares approach [78]. The aforementioned merits in terms of efficiency and accuracy makes Kriging an ideal metamodeling choice as compared to the alternatives discussed in the introduction, e.g., polynomial schemes and neural networks. These properties ensure, that once calibrated, the Kriging metamodel possess the efficiency that will enable real-time damage assessment while maintaining the fidelity and resolution of the framework outlined in Section 3. A summary of the calibration process is as follows:

1. *Design of experiments*: Select a set of samples/support points within the input space, i.e., the space defined by $\mathbf{x} = [v_H, \alpha]^{\mathrm{T}}$.
2. *Data collection*: For each of the support points, carry out a high-fidelity damage assessment as outlined in Section 3 and evaluate the conditional statistics of the damage measures defined in Section 4.1. As such, the training set $\mathbf{S}$ is formulated by pairing the outputs (the conditional statistics $\mu_{D_C|v_H,\alpha}$ and $\sigma_{D_C|v_H,\alpha}$) with the corresponding support points.
3. *Kriging calibration*: The Kriging metamodel is calibrated by solving Eqs. (25)-(27) through an appropriate algorithm, e.g., the highly efficient and robust Design and Analysis of Computer Experiments (DACE) toolbox [79], for each conditional statistic of each damage state of each envelope component.
4. *Kriging validation*: The accuracy of the calibrated Kriging metamodels (one for each damage state of each envelope component) are tested by making predictions on a set of inputs not used during calibration. The accuracy is measured through the difference between the Kriging predictions and the ground truth outputs calculated from the high-fidelity model. If satisfactory accuracy is achieved, the calibrated Kriging metamodels are accepted. If the accuracy is not deemed sufficient, the four steps outlined above are

repeated for an adjusted design of experiments and/or Kriging configuration (e.g., the choice of $R(\mathbf{x}, \mathbf{x}', \boldsymbol{\theta})$).

5. Real-time damage risk forecast

By assuming that the conditional probabilities, $P(D_C|v_H, \alpha)$, can be described by an appropriate two parameter distribution, the Kriging metamodels for $\mu_{D_C|v_H,\alpha}$ and $\sigma_{D_C|v_H,\alpha}$ can be used to directly estimate $P(D_C|v_H, \alpha)$. From the knowledge of $P(D_C|v_H, \alpha)$, the unconditional risk of damage, $P(D_C < 0)$, for each envelope component and damage state of the building system, can be directly evaluated through the law of total probability as:

$$P(D_C < 0) = \iint_{v_H,\alpha} P(D_C < 0|v_H, \alpha)p(v_H, \alpha)dv_H d\alpha \tag{28}$$

where $p(v_H, \alpha)$ is the joint probability density function between v_H and α while $P(D_C < 0|v_H, \alpha)$ is the conditional probability of $\{D_C : D_C < 0\}$, i.e., of damage. In practice, by generating in real-time N samples of v_H and α belonging to $p(v_H, \alpha)$ through the forecast model of Section 2.2, Eq. (28) can be directly estimated through Monte Carlo simulation as:

$$P(D_C < 0) \approx \frac{1}{N} \sum_{i=1}^{N} P(D_C < 0|v_{H,i}, \alpha_i) \tag{29}$$

were $v_{H,i}$ and α_i for $i = 1, 2, ..., N$ are the samples belonging to $p(v_H, \alpha)$.

The risk of damage of Eq. (29) can be seen as a direct measure of disaster consequence and provides powerful information in support to early emergency response and management. Figure 2 presents an overview flowchart of the proposed risk forecasting framework for envelope systems of engineered buildings. It should be noted that this framework can be applied to portfolios of engineered buildings, e.g., all the critical facilities of a given county, as the Kriging metamodels can be completely calibrated offline.

6. Case study

6.1. The building system

A rectangular 45-story building located in Miami, Florida, is considered as a case study (Figure 3a). The total height of the building is 180 m, with each story height 4 m. The

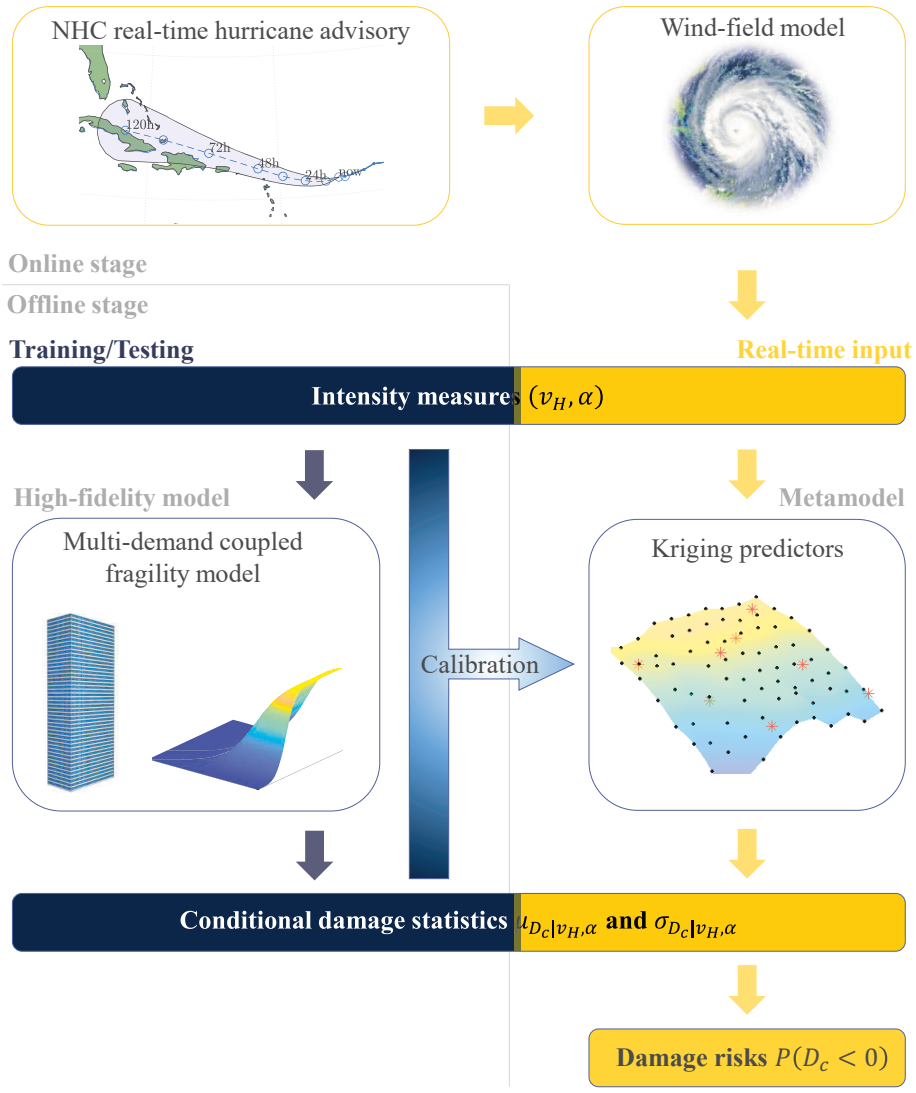

Figure 2: Schematic of the proposed real-time damage risk forecasting framework.

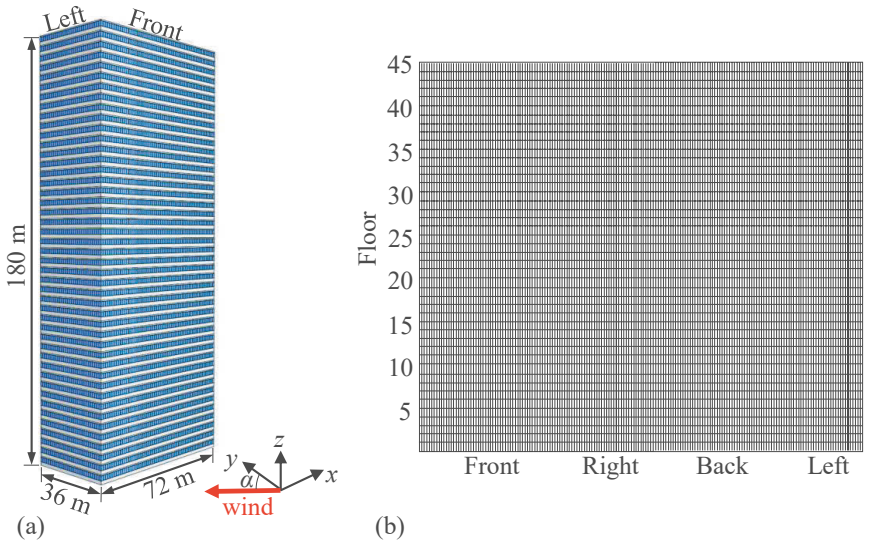

Figure 3: The case study building: (a) 3D view; (b) the unfolded envelope system.

building's structural system is a steel braced frame with box sections for columns and W24 sections (standard American Institute for Steel Construction (AISC) members) for beams and braces. The structure was designed to meet the requirement of interstory drift ratios not exceeding 1/400 under a wind speed with mean recurrence interval (MRI) of 50 years and to have all members remaining linear elastic for wind speeds with MRIs of 1700 years. In addition to the structural mass, a carried mass of 0.38 t/m^2 at each floor level was considered. As a result, the first three natural frequencies of the structure were 1.30, 1.67, and 2.70 rad/s, respectively. For the dynamic response analyses, the first 10 vibration modes were considered sufficient. In integrating the modal equations, the modal damping ratios were considered fully correlated with uncertainty describe by a lognormal distribution with mean 1.4% and coefficient of variation of 0.3. The stochastic pressure model of Section 3.1 was calibrated to datasets of the Tokyo Polytechnic University wind pressure database [80]. This data was used to estimate the spectral POD eigenvalues and eigenvectors of Eq. (12). The first 10 spectral modes were considered sufficient for representing the external pressure field. The kernal-Pareto mixture model of the marginal distributions of the pressure coefficients were calibrated considering 5% upper and lower tail thresholds.

The envelope system consists of a total of 8,100 damageable glazing components, with 180 elements on each floor (Figure 3b). Each of the envelope components is composed of an

Table 1: Parameters of fragility functions.

Damage state	Phenomenon	Median	Dispersion	Mean	Std
DS_1^{Dr} (rad)	Hair-line crack	0.021	0.45	-	-
DS_2^{Dr} (rad)	Crack	0.024	0.45	-	-
DS^p (kPa)	Blow-out	-	-	5.29	0.91

internal and external laminated glass pane, both with a size of 1.2 m $\times$ 2 m and thickness of 6 mm. Each envelope component was assumed to be susceptible two drift induced damage states, DS_1^{Dr} and DS_2^{Dr} respectively, and one pressure-induced damage state, DS^p. The drift induced damage states physically refer to the occurrence of hair-line cracking or cracking of the laminated glass panes, while the pressure induced damage state refers to glass blow-out. In evaluating p_{eq}, t_{eq} and s were taken respectively as 60 s and 16 in Eq. (17). The parameters of the fragility functions describing the uncertainties in the damage states are summarized in Table 1 [81, 82]. In addition, to account for the coupling between the occurrence of a drift induced damage state and the reduction in the capacity of the component to resist net pressure, a random reduction factor ρ_{C^p} is considered for C^p. In particular, it is assumed that ρ_{C^p} follows a truncated normal distribution in $[0, 1]$ with a coefficient of variance of 0.1. The mean reduction in capacity to resist net pressure upon occurrence of DS_1^{Dr} or DS_2^{Dr} was set to 90% and 10% respectively.

6.2. Kriging-based rapid damage assessment: Offline stage

6.2.1. Kriging training

A high-fidelity training dataset, $\mathbf{S}$, was simulated through the framework in Section 3. In particular, the support points $\mathbf{x}_i = (v_{H,i}, \alpha_i)$ were generated through a grid sampling plan defined by α belonging to the discrete set $\{0^\circ,\ 10^\circ, ...,\ 350^\circ\}$ and the axis of v_H divided into three, five, three equispaced intervals of ranges 0 m/s to 43.90 m/s (MRI = 50 years), 43.90 m/s to 75.66 m/s (MRI = 10^7 years), and 75.66 m/s to 94.70 m/s (MRI = 10^{13} years), as shown in Figure 4. The data grid is denser for higher v_H where stronger nonlinearity is expected in the Kriging metamodel. Further, it should be noted that α is bounded, and thus the training dataset is augmented by adding a grid at $\alpha = 360^\circ$, with data copied from $\alpha = 0^\circ$. Within this context, a total of $n_{\mathbf{x}} = 444$ support points were generated for

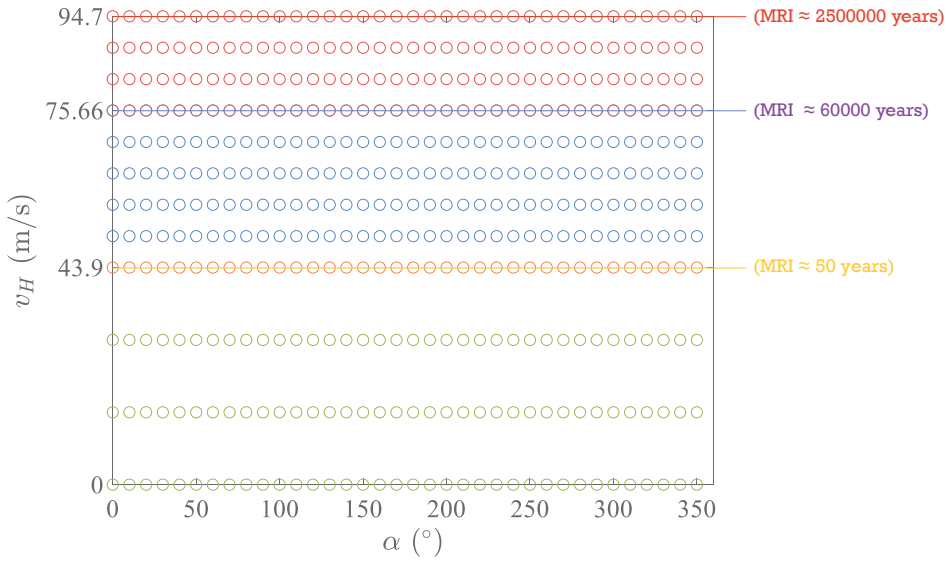

Figure 4: The training dataset (support points) and the testing dataset.

the Kriging training. At each of the support points, the first two conditional moments, i.e., $\mu_{D_C|v_H,\alpha}$ and $\sigma_{D_C|v_H,\alpha}$, were estimated for all 24,300 potential damage states (8,100 envelope components with three damage states each) of the envelope system. To this end, Monte Carlo simulations were carried out using 1,000 samples at each support point from which $\mu_{D_C|v_H,\alpha}$ and $\sigma_{D_C|v_H,\alpha}$ were directly estimated for all 24,300 potential damage states.

In defining a Kriging metamodel, the selection of the correlation function $R(\mathbf{x}, \mathbf{x}', \boldsymbol{\theta})$ is critical to accurate predictions. To this end, the commonly used forms summarized in Table 2 will be comparatively discussed so as to determine the most appropriate correlation function for the applications of this work. The second-order polynomial bases $\mathbf{g}(v_H, \alpha) = [1,\ v_H, \alpha, v_H^2,\ v_H\hat{\alpha},\ \alpha^2]$ was considered to enable a reasonable extrapolation at inquiry points that fall outside of the range covered by the support points. Within this context, a single output Kriging predictor is calibrated for each of the three pairs of damage statistics, i.e., $(\mu_{D_{C_1^{Dr}}|v_H,\alpha}, \sigma_{D_{C_1^{Dr}}|v_H,\alpha})$, $(\mu_{D_{C_2^{Dr}}|v_H,\alpha}, \sigma_{D_{C_2^{Dr}}|v_H,\alpha})$, and $(\mu_{D_{C^p}|v_H,\alpha}, \sigma_{D_{C^p}|v_H,\alpha})$, for the 8,100 envelope components. Calibration was performed through the DACE toolbox [79]. The computational effort is measured in terms of the total time elapsed in learning the damage statistics for all 8,100 envelope components in the training set. A comparative summary is reported in Table 3. It is seen that the spherical correlation function is the most efficient for calibrating. Note that all computations of this work were performed on a personal computer

Table 2: Correlation functions considered in calibrating the Kriging metamodel.

Function	R_j
Exponential	$\exp\left(-\theta_j\lvert x_j - x'_j\rvert\right)$
Generalized exponential	$\exp\left(-\theta_j\lvert x_j - x'_j\rvert^{\theta_{n+1}}\right)$
Gaussian	$\exp\left(-\theta_j\lvert x_j - x'_j\rvert^2\right)$
Linear	$\max\{0,\ 1-\theta_j\lvert x_j - x'_j\rvert\}$
Spherical	$1-1.5\eta_j+0.5\eta_j^3,\ \eta_j=\min\{1,\ \theta_j\lvert x_j - x'_j\rvert\}$
Spline	$\begin{cases} 1-15\eta_j^2+30\eta_j^3,\ \eta_j\in[0,0.2] \\ 1.25(1-\eta_j)^3,\ \eta_j\in(0.2,1) \\ 0,\ \eta_j\in[1,+\infty) \end{cases}, \eta_j=\theta_j\lvert x_j - x'_j\rvert$

Note: $R(\mathbf{x},\mathbf{x}',\boldsymbol{\theta})=\prod_{j=1}^{n} R_j$.

Table 3: The computational effort measured by elapsed time during training (in seconds).

Kernel	$\mu_{D_{C_1^{Dr}}\lvert v_H,\alpha}$	$\sigma_{D_{C_1^{Dr}}\lvert v_H,\alpha}$	$\mu_{D_{C_2^{Dr}}\lvert v_H,\alpha}$	$\sigma_{D_{C_2^{Dr}}\lvert v_H,\alpha}$	$\mu_{D_{C^p}\lvert v_H,\alpha}$	$\sigma_{D_{C^p}\lvert v_H,\alpha}$
Exponential	382.16	282.69	366.70	281.84	306.86	356.07
Generalized exponential	434.18	411.47	410.63	406.51	940.09	451.07
Gaussian	333.22	322.46	320.46	319.45	309.77	319.45
linear	128.78	115.22	121.68	108.77	222.99	<u>145.13</u>
Spherical	<u>121.91</u>	<u>100.45</u>	<u>118.51</u>	<u>100.52</u>	<u>199.49</u>	164.72
Spline	197.61	144.92	186.53	144.33	287.34	268.02

Note: Minimum training times indicated with underlining.

with Intel(R) with i7-8700 Core(TM) with 32 GB RAM.

6.2.2. Kriging testing

To test the generality of the calibrated Kriging predictor, a testing dataset composed of $n'_{\mathbf{x}} = 60$ random samples was considered (asterisks in Figure 4). The average mean error (AME) [78] is considered to quantify the accuracy:

$$AME = \frac{1}{n_{\mathrm{e}}}\sum_{k=1}^{n_{\mathrm{e}}}\left[\frac{\sum_{i=1}^{n'_{\mathbf{x}}}\left|y'_i(\mathbf{x}'_i;\bar{\boldsymbol{\xi}}_k)-\hat{y}'_i(\mathbf{x}'_i;\bar{\boldsymbol{\xi}}_k)\right|}{\sum_{i=1}^{n'_{\mathbf{x}}}\left|y'_i(\mathbf{x}'_i;\bar{\boldsymbol{\xi}}_k)\right|}\right] \tag{30}$$

where $k = 1, 2, ..., n_{\mathrm{e}}$ are the indices of the envelope elements, and $n_{\mathrm{e}} = 8,100$ in this case. This error measure is defined to reflect the global performance of the predictor in reproducing a certain damage statistic for all envelope elements and testing samples. The AME by Kriging considering each of the correlation functions is summarized in Table 4. In

Table 4: Prediction accuracy measured by AME over the testing dataset.

Kernel	$\mu_{D_{C_1^{Dr}}\|v_H,\alpha}$	$\sigma_{D_{C_1^{Dr}}\|v_H,\alpha}$	$\mu_{D_{C_2^{Dr}}\|v_H,\alpha}$	$\sigma_{D_{C_2^{Dr}}\|v_H,\alpha}$	$\mu_{D_{C^p}\|v_H,\alpha}$	$\sigma_{D_{C^p}\|v_H,\alpha}$
Exponential	1.77%	3.38%	1.72%	3.38%	0.76%	2.57%
Generalized exponential	1.79%	3.90%	1.74%	3.91%	0.76%	2.59%
Gaussian	3.07%	5.60%	2.89%	5.60%	4.70%	5.97%
linear	1.87%	3.82%	1.83%	3.82%	0.77%	2.65%
Spherical	1.81%	3.27%	1.75%	3.27%	0.76%	2.58%
Spline	2.04%	3.25%	1.95%	3.25%	0.84%	2.94%

addition, the Kriging surfaces and predicted values of $\mu_{D_C|v_H,\alpha}$ and $\mu_{D_C|v_H,\alpha} \pm \sigma_{D_C|v_H,\alpha}$ for a representative envelope component are compared to the high-fidelity data in Figure 5. Except for the Gaussian correlation function, all other correlation functions yield similar results to the spherical kernel and are therefore omitted from Figure 5 for clarity of presentation. The prediction accuracy demonstrated in Figure 5 is consistent with Table 4. It is seen from Table 4 that overall the exponential correlation shows the best accuracy, while the spherical correlation exhibited similar performance. However, the most widely used Gaussian correlation performs the worst among the considered correlation functions. It can be observed from the Kriging surfaces in Figure 5 that the predictor using the Gaussian correlation is showing an erroneous fluctuation around lower wind speeds. This fluctuation is the major reason for the worst performance of the Gaussian correlation function. In addition, the simulation efficiency relative to the high-fidelity damage assessment framework is shown in Table 5, where all the correlation functions enable the Kriging metamodel to be more than four orders of magnitude faster than the high-fidelity framework. In particular, the linear correlation function is seen to have the highest efficiency, which is reasonable as it is the simplest in terms of function operations. The exponential and spherical correlation functions are seen to have similar efficiency, with both accelerating the damage evaluation by more than 30,000 folds. The spline correlation is seen to have the lowest efficiency due to the more complex operations involved. Overall, the spherical correlation is excellent in training, simulation efficiency, as well as accuracy, and thus will be adopted in the following online stage, i.e., real-time forecast.

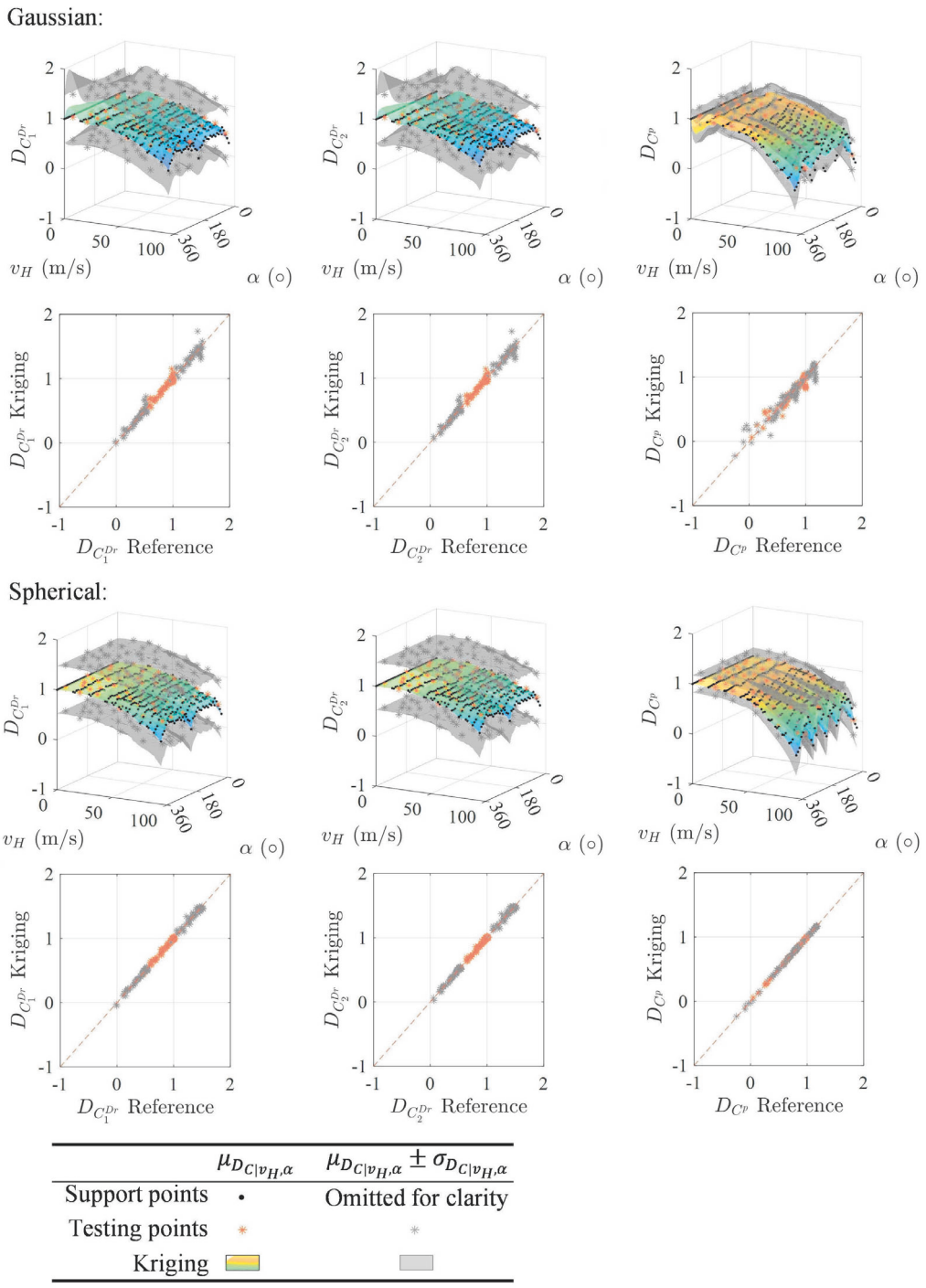

Figure 5: The Kriging surfaces and predicted values of $\mu_{D_C|v_H,\alpha}$ and $\mu_{D_C|v_H,\alpha} \pm \sigma_{D_C|v_H,\alpha}$ compared to the high-fidelity data. The results shown are for the 20th (count from the left) envelope element at the 10th floor of the front face of the building of Figure 3(b).

Table 5: Comparison of the simulation efficiency between the high-fidelity and Kriging models over the testing dataset.

Kernel	High-fidelity	Kriging	Speed-up by
Exponential	15.45 days	42.26 sec	31,578
Generalized exponential		52.22 sec	25,559
Gaussian		44.58 sec	29,946
linear		39.03 sec	34,196
Spherical		42.62 sec	31,317
Spline		78.71 sec	16,956

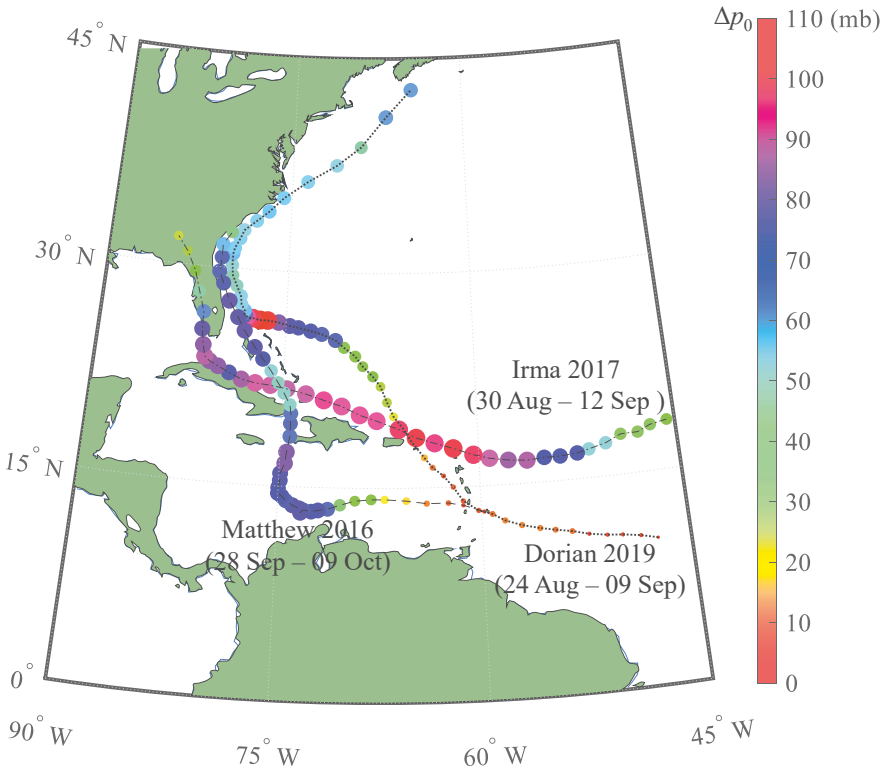

Figure 6: Best tracks and pressure deficits of the three considered historical hurricanes.

6.3. Real-time damage forecast: Online stage

To demonstrate the applicability of the calibrated Kriging metamodel for real-time damage risk forecasting, three historical hurricanes that impacted Florida, namely hurricane Matthew in 2016 [83], hurricane Irma in 2017 [84], and hurricane Dorian in 2019 [85], are considered. The intensity of each hurricane is described through the evolution of the pressure deficit, Δp_0. This is reported in Figure 6 together with the best track estimate. In this section, with the calibrated Kriging metamodel, the proposed framework is firstly implemented for the three hurricanes, with results reported in Section 6.3.1. Further, validations to justify the risk evaluations are provided in the subsequent Section 6.3.2.

6.3.1. Forecast results

To implement the framework, the site-specific wind intensity is forecast every six hours from when the hurricane event begins. The forecast is based on the scheme outlined in Section 2 and therefore the real-time advisories issued by NHC during the hurricane events. In particular, for the scheme outlined in Section 2, the Holland number was taken as $B = 1.5$, the boundary layer thickness was taken as $h = 1000$ m, and the diffusion coefficient was taken as $K = 0.5\kappa^2 Bvr$ with $\kappa = 0.4$ [59]. In addition, the deflection coefficient was taken as $\alpha_M = \tan(20^\circ)$. The environmental length scale r_{G} in Eq. (8) was taken as 500 km. For the wind speed transformation of Eq. (9), the terrain roughness length at the site of interest and the meteorological station were respectively $z_0 = 1.28$ m and $z_{01} = 0.03$ m, while the height at the building top and the meteorological station were $H = 180$ m and $H_{\mathrm{met}} = 10$ m. The empirical constant was taken as $\delta = 0.0706$. Within this context, samples of the forecast site-specific wind intensity were generated every six hours, and input into the calibrated Kriging metamodel to predict for the conditional damage statistics. These were used to calibrate prescribed conditional distribution functions for $P(D_C|v_H, \alpha)$ and the damage risks of all envelope elements were subsequently evaluated through Eq. (29). In particular, based on experience, the prescribed conditional distribution functions for $P(D_C|v_H, \alpha)$ were assumed as shifted lognormal distributions for drift-induced damage and normal distributions for pressure-induced damage. Following these assumptions, the conditional probability of a

given envelope component damage state can be written as:

$$P(D_C < 0 | v_H, \alpha) = \Phi\left(\frac{l-m}{s}\right) \tag{31}$$

with $\Phi(\cdot)$ the standard normal distribution function and where for one of the two ($i = 1, 2$) drift-induced damage states: $l = \ln(1 - \mu_{D_{C_i^{Dr}}|v_H,\alpha})$, $m = -\ln\left(\sqrt{\sigma^2_{D_{C_i^{Dr}}|v_H,\alpha} + 1}\right)$, and $s = \sqrt{\ln(\sigma^2_{D_{C_i^{Dr}}|v_H,\alpha} + 1)}$; while for the pressure-induced damage state: $l = 0$, $m = \mu_{D_{C^p}|v_H,\alpha}$, and $s = \sigma_{D_{C^p}|v_H,\alpha}$.

In terms of uncertainty, in addition to the randomness of the structural properties, capacities, stochasticity of the wind loads, and storm tracks, the radius to the maximum wind, r_M, and filling model of Eq. (7), through the parameter ϵ, are considered as uncertain with r_M following a lognormal distribution and ϵ a normal distribution [86, 65]. Additionally, the current central pressure deficit Δp_0 is assumed to follow a normal distribution, with mean set to the value of Δp_0 obtained from the real-time hurricane advisory and standard deviation set to 9.5 mb, as suggested in [87].

Through the developed framework, real-time probabilistic damage forecasts during the entire lifetime of the three hurricanes were generated. The framework was used to provide forecasts up to five days ahead. In particular, forecasts for three and five days ahead for hurricane Matthew (2016), Irma (2017), and Dorian (2019) are shown in Figures 7, 8, and 9, respectively. The five day forecast for hurricane Matthew and Dorian are not included as the damage risks were seen to be negligible. The results contain comprehensive information on the likelihood of an envelope component experiencing damage ranging form glazing unit cracking to complete blowout. For example, from Figure 8 and the five day damage forecast, it can be seen that there is around a 1% chance of window blowout on the right edge of the right face of the building. The subsequent three day damage forecast shows how the 1% chance of window blowout has now extended to include the right edge of the left face. The computational time to generate/update these results was eight minutes on the desktop computer of Section 6.2.1. This efficiency clearly illustrates the potential of the approach as a real-time damage risk framework. The comprehensive information of damage risk to the building envelope would allow disaster managers to order preventative measures to be implemented or evacuation of personnel and equipment to be performed ahead of time in

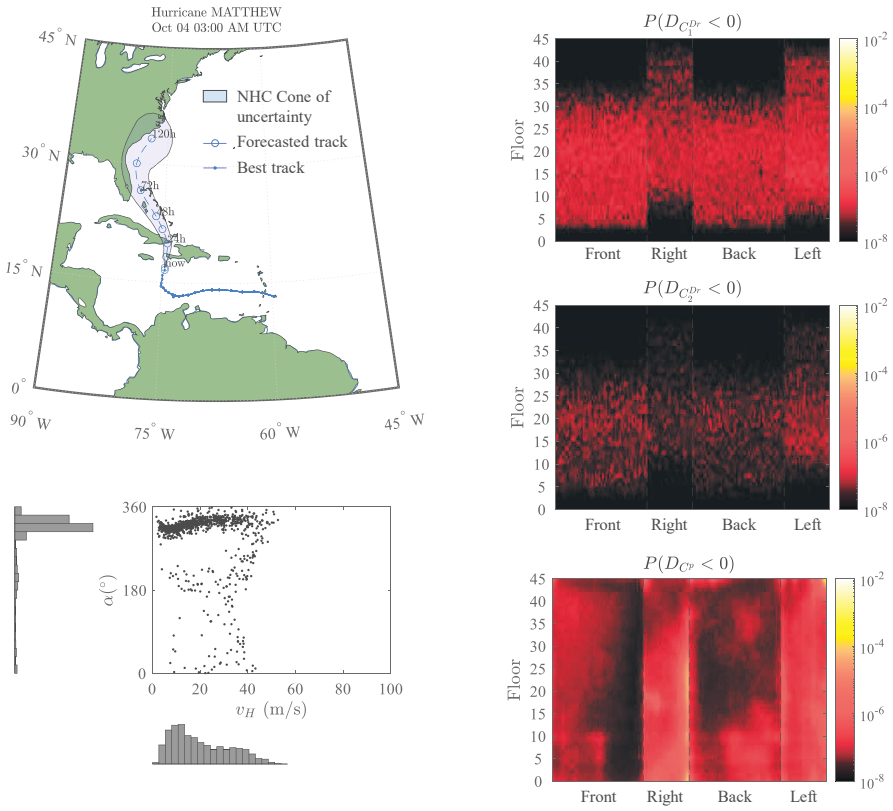

Figure 7: Real time damage forecast on Oct 04 at 03:00 AM UTC (3 days ahead) for envelope components during hurricane Matthew.

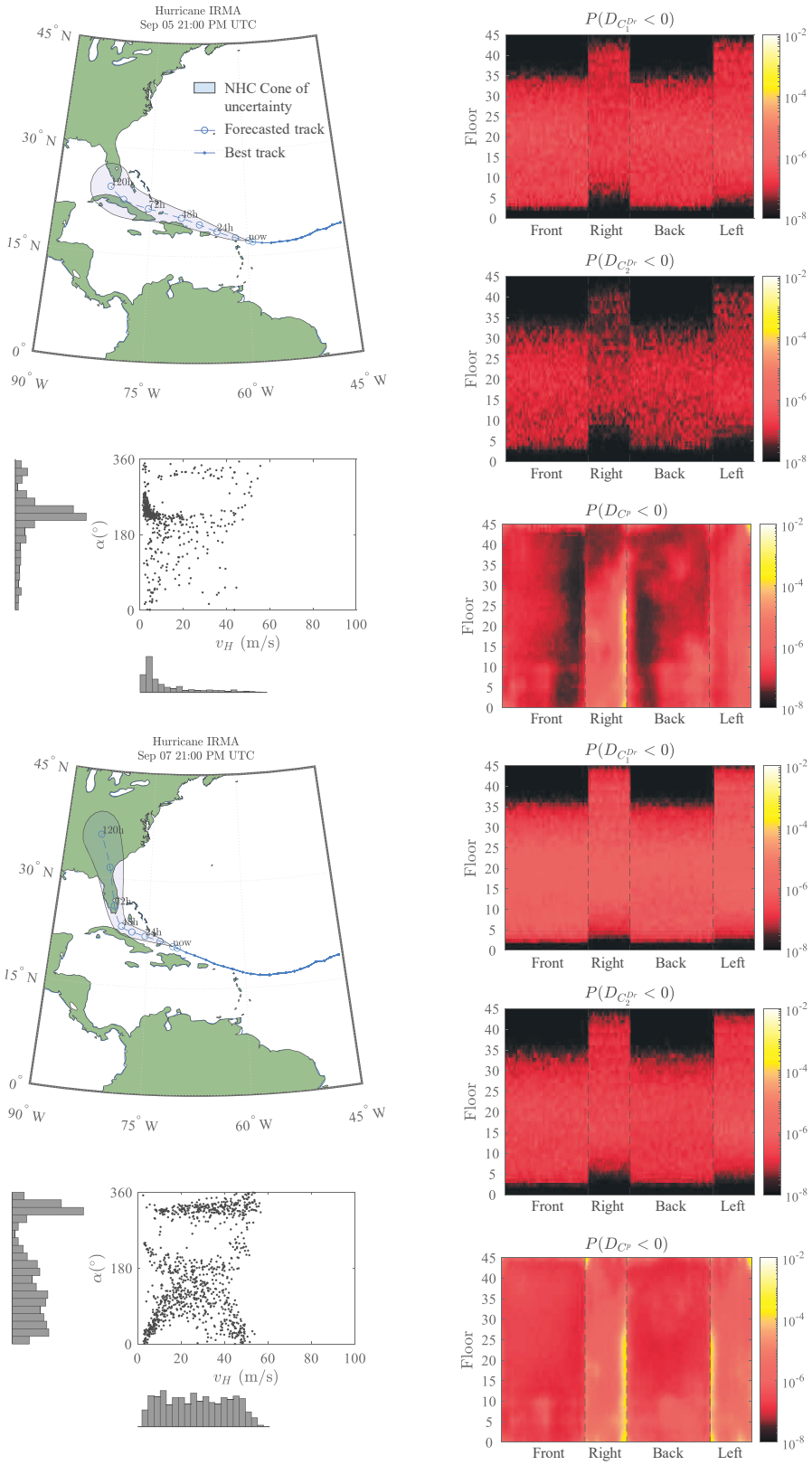

Figure 8: Real time damage forecast on Sep 05 at 21:00 PM UTC (5 days ahead) and Sep 07 21:00 PM UTC (3 days ahead) for envelope components during hurricane Irma.

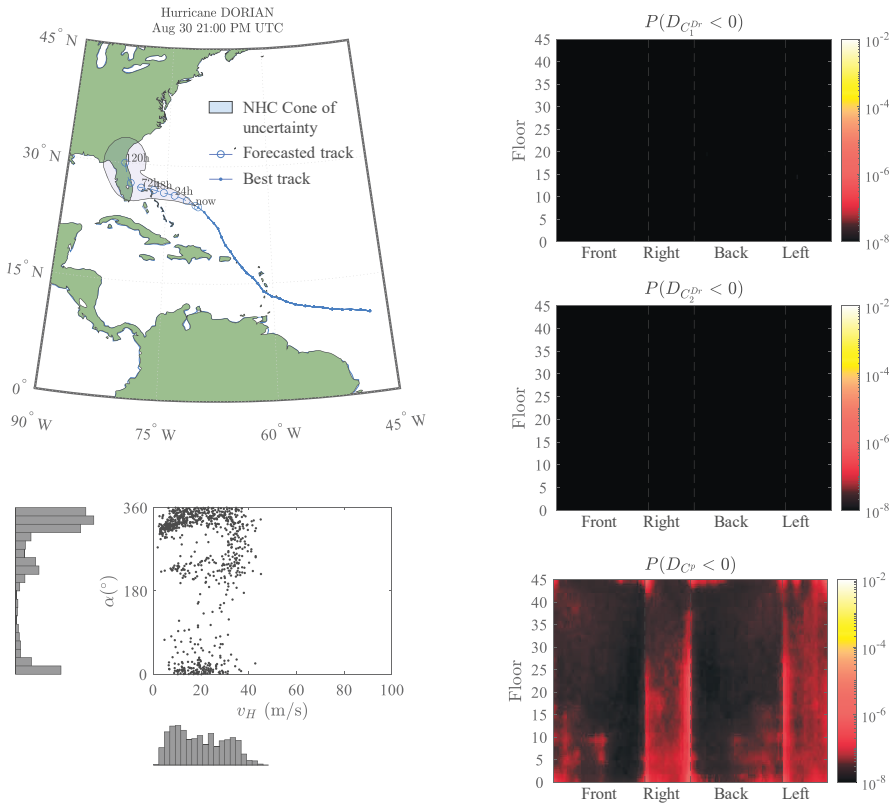

Figure 9: Real time damage forecast on Aug 30 at 21:00 PM UTC (3 days ahead) for envelope components during the hurricane Dorian.

certain parts of the building or, if deemed necessary, the entire building.

6.3.2. Validation of the real-time damage forecast model

The hurricane track model adopted in the real-time damage forecast framework of this work has already been validated by NHC [62]. The discrepancies seen in this validation are treated as a source of uncertainty through the random variables e_{ϕ,t_T} and e_{λ,t_T}. In addition, the parametric wind field model has been carefully validated [59, 88] and serves as the basis of the ASCE 7 wind maps. Notwithstanding how the validity of the Kriging metamodels for predicting the conditional damage statistics is demonstrated in Section 6.2.2, the accuracy of the assumed distributions, $p(D_C|v_H, \alpha)$, for the conditional damage measures (based on which the risk is evaluated) requires investigation. This section studies, therefore, the accuracy of reconstructing $p(D_C|v_H, \alpha)$ from the damage statistics, i.e., $\mu_{D_C|v_H,\alpha}$ and $\sigma_{D_C|v_H,\alpha}$. To evaluate the accuracy, Pearson's χ^2 test and Kullback–Leibler (KL) divergence measure are considered. In particular, Pearson's χ^2 test examines how the observed frequency

distribution, estimated from n samples of the high-fidelity model, differs from the assumed distribution, with the difference measured by the test statistic:

$$\chi^2 = \sum_{i=1}^{k} \frac{(O_i - E_i)^2}{E_i} \tag{32}$$

where k is the total number of mutually exclusive classes, O_i are the observations of the high-fidelity model in class i, while E_i is the expected number of observations (based on the total number of simulated samples n and the assumed distribution) in class i. The test statistic is then compared with a critical value derived from the chi-squared distribution at a designated significance level, which, as in this work, is typically taken as 5%. The assumed distribution is accepted (binary indicator $h = 0$) if χ^2 is lower than the critical value, and rejected ($h = 1$) otherwise. In addition, KL divergence provides a supplementary measure of the difference in logarithmic scale, which can be taken as the expected excess surprise from using the assumed distribution:

$$d_{\mathrm{KL}} = \sum_{i=1}^{k} \frac{O_i}{n} \log\left(\frac{O_i}{E_i}\right) \tag{33}$$

The goodness of fit measures introduced in Eqs. (32)-(33) were estimated for all damage states of each envelope component for the hurricane cases considered in Section 6.3.1. The validation results are shown in Figures 10-13 in the form of contour plots, where the rejection rates of h and the expected value of d_{KL} over all envelope components, indicated as $\bar{h}$ and $\bar{d}_{\mathrm{KL}}$, are estimated for the three possible damage states. In estimating the contours, 1000 high-fidelity samples were used following the wind speed and direction grid of Figure 4 with domain extension estimated from the wind speed and direction samples forecast for each event. It is seen from Figures 10-13 that, despite some variability, $\bar{h}$ is generally around 5% while $\bar{d}_{\mathrm{KL}}$ is around 0.003. This is confirmed in Table 6 that reports the average value of $\bar{h}$ and $\bar{d}_{\mathrm{KL}}$ over the wind speed and direction domains of each event forecast. As can been seen, all average values are under 5% and 0.003. These results attest to the overall adequacy of the probability distributions assumed for the real time risk evaluations of this work.

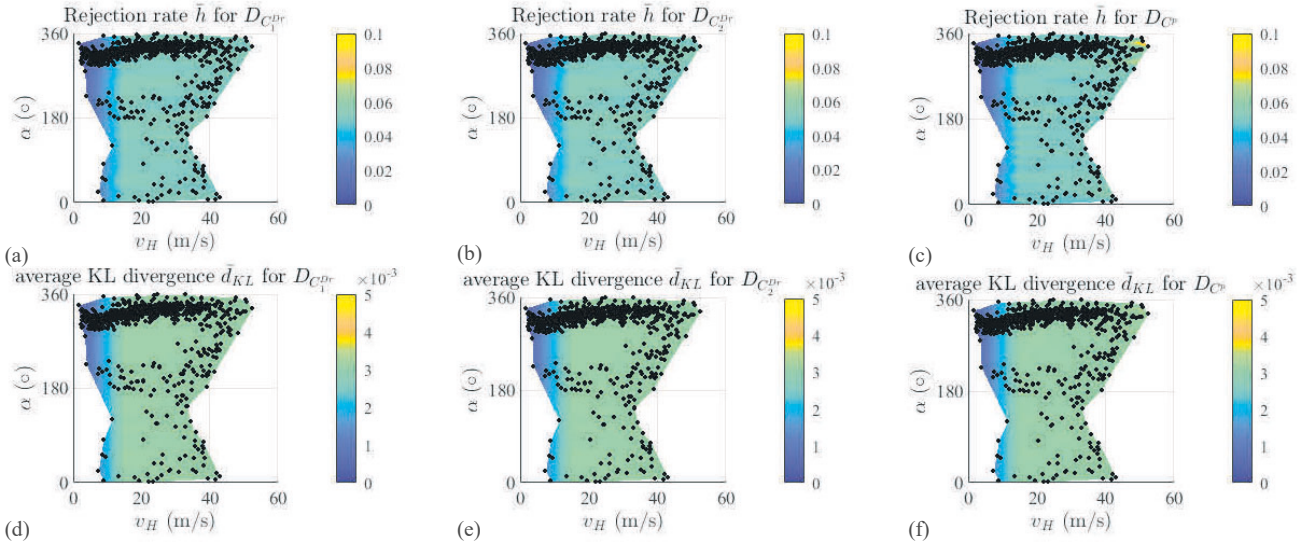

Figure 10: Contour maps of $\bar{h}$ and $\bar{d}_{\mathrm{KL}}$ for the forecast of Oct 04 at 03:00 AM UTC (3 days ahead) during hurricane Matthew: (a)-(c) rejection rates for damage states $D_{C_1^{Dr}}$, $D_{C_2^{Dr}}$, and D_{C^P}; (d)-(f) average KL divergence for damage states $D_{C_1^{Dr}}$, $D_{C_2^{Dr}}$, and D_{C^P}.

Table 6: Average rejection rates and KL divergence.

	Average rejection rate			Average KL divergence		
Damage states	$D_{C_1^{Dr}}$	$D_{C_2^{Dr}}$	D_{C^P}	$D_{C_1^{Dr}}$	$D_{C_2^{Dr}}$	D_{C^P}
Matthew, 3 Days ahead	4.8217%	4.8222%	4.7350%	0.002845	0.002845	0.002835
Irma, 5 Days ahead	4.5407%	4.5362%	4.5195%	0.002682	0.002682	0.002678
Irma, 3 Days ahead	4.7415%	4.7372%	4.7417%	0.002797	0.002797	0.002796
Dorian, 3 days ahead	4.6115%	4.6131%	4.5039%	0.002723	0.002723	0.002711

7. Conclusion

In this paper, a metamodel-driven real-time risk forecast framework for hurricane-induced building damage was outlined for the envelope systems of engineered buildings. The framework consists of a scheme for site-specific wind intensity forecasting and the Kriging metamodeling technique for rapid probabilistic damage quantification. In particular, with high-fidelity damage being simulated through a recently developed probabilistic multi-demand progressive and coupled fragility model, the Kriging metamodeling technique is introduced as a surrogate to gain the efficiency needed for real-time applications. The Kriging metamodel, once calibrated, is further used in Monte Carlo simulations for rapidly estimating

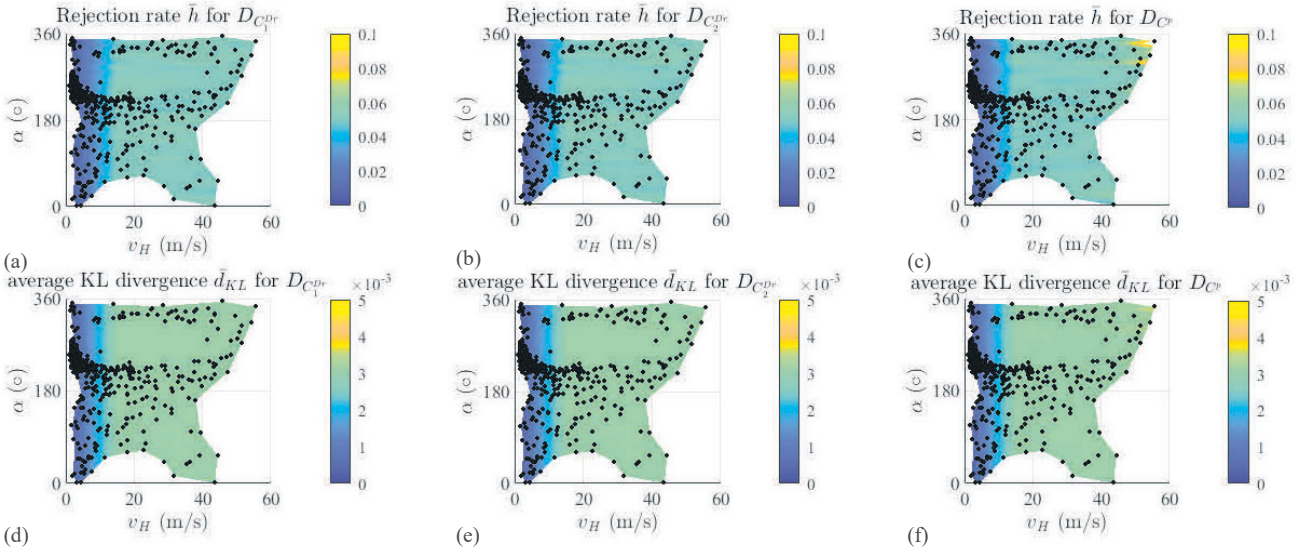

Figure 11: Contour maps of $\bar{h}$ and $\bar{d}_{\mathrm{KL}}$ for the forecast of Sep 05 at 21:00 PM UTC (5 days ahead) during hurricane Irma: (a)-(c) rejection rates for damage states $D_{C_1^{Dr}}$, $D_{C_2^{Dr}}$, and D_{C^p}; (d)-(f) average KL divergence for damage states $D_{C_1^{Dr}}$, $D_{C_2^{Dr}}$, and D_{C^p}.

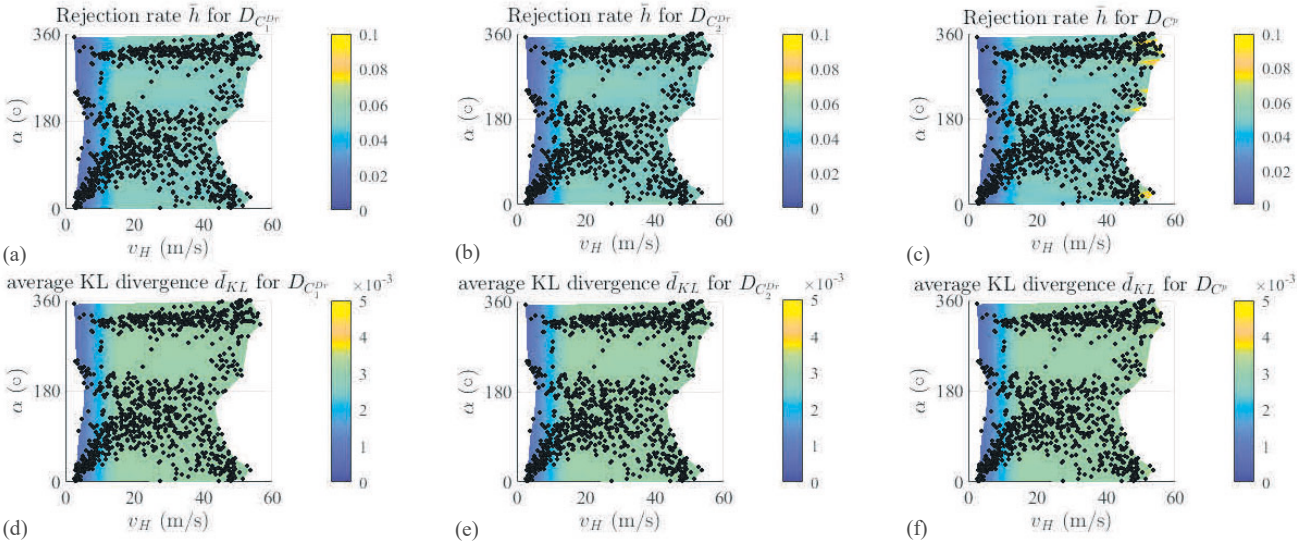

Figure 12: Contour maps of $\bar{h}$ and $\bar{d}_{\mathrm{KL}}$ for the forecast of Sep 07 at 21:00 PM UTC (3 days ahead) during hurricane Irma: (a)-(c) rejection rates for damage states $D_{C_1^{Dr}}$, $D_{C_2^{Dr}}$, and D_{C^p}; (d)-(f) average KL divergence for damage states $D_{C_1^{Dr}}$, $D_{C_2^{Dr}}$, and D_{C^p}.

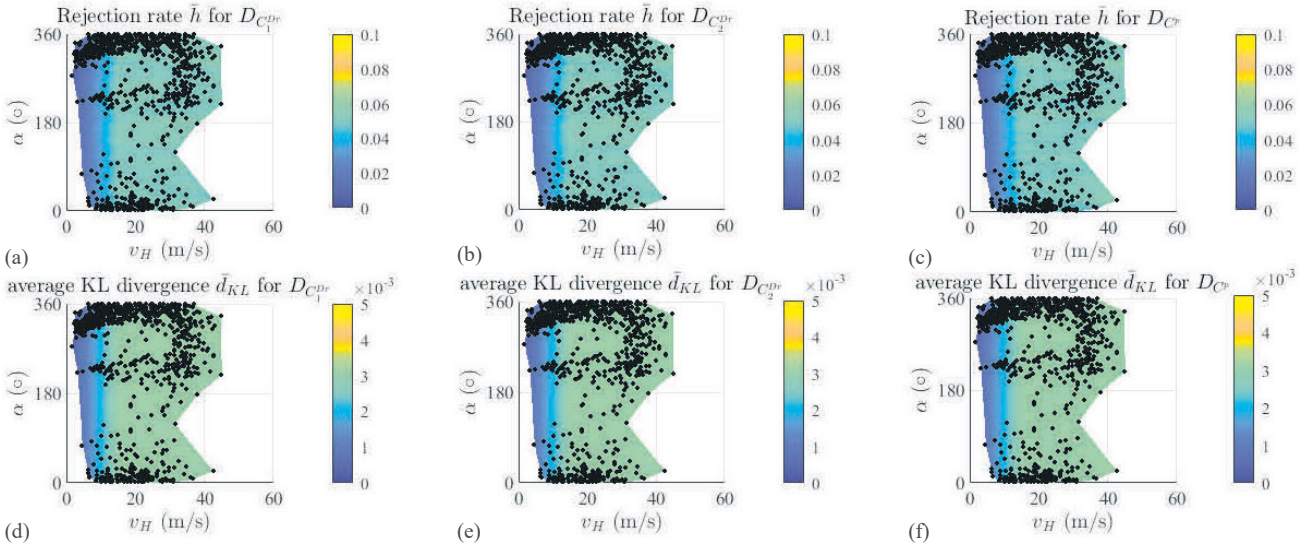

Figure 13: Contour maps of $\bar{h}$ and $\bar{d}_{\mathrm{KL}}$ for the forecast of Aug 30 at 21:00 PM UTC (3 days ahead) during the hurricane Dorian: (a)-(c) rejection rates for damage states $D_{C_1^{Dr}}$, $D_{C_2^{Dr}}$, and D_{C^p}; (d)-(f) average KL divergence for damage states $D_{C_1^{Dr}}$, $D_{C_2^{Dr}}$, and D_{C^p}.

damage risk from real time forecasts of site-specific wind intensity of an imminent hurricane obtained by integrating real-time hurricane advisories with parametric wind field models. The efficiency and applicability of the developed framework was illustrated through a case study consisting in a 45-story building located in Miami, Florida. Through a comparative study, it was found that Kriging with spherical correlation function has the best overall performance for the applications of this work. This Kriging configuration, once calibrated, can predict the second order conditional damage statistics associated with each component of a envelope system with remarkable accuracy and with an efficiency gain of more than four orders of magnitude as compared to the high-fidelity reference solution. Subsequently, with the calibrated Kriging metamodel, real-time forecast of damage risks is successfully demonstrated by considering the real-time advisories of three historical hurricane events. The efficiency and accuracy of the developed framework demonstrates its potential as a decision support tool for emergency response and management of buildings in hurricanes prone regions. Moreover, the framework can be extended to portfolios of buildings or infrastructures therefore defining a regional real-time hurricane-induced damage alert framework.

Acknowledgements

The research effort was supported in part by the National Science Foundation (NSF) under Grant CMMI-1750339 as well as the University of Michigan's Mcubed 3.0 program. This supports are gratefully acknowledged.

References

[1] Emanuel, K.. Increasing destructiveness of tropical cyclones over the past 30 years. Nature 2005;436(7051):686–688.

[2] Reidmiller, D.R., Avery, C.W., Easterling, D.R., Kunkel, K.E., Lewis, K.L.M., Maycock, T.C., et al. Fourth national climate assessment. Volume II: Impacts, risks, and adaptation in the United States. Tech. Rep.; US Global Change Research Program; 2019.

[3] Bevere, L., Gloor, M.. sigma 2/2020: Natural catastrophes in times of economic accumulation and climate change. Tech. Rep.; Swiss Reinsurance; 2020.

[4] Abdelhady, A.U., Spence, S.M.J., McCormick, J.. A framework for the probabilistic quantification of the resilience of communities to hurricane winds. Journal of Wind Engineering and Industrial Aerodynamics 2020;206:104376.

[5] National Oceanic and Atmospheric Administration (NOAA). National coastal population report: Population trends from 1970 to 2020. Tech. Rep.; National Oceanic and Atmospheric Administration (NOAA); 2013.

[6] Powell, M.D., Houston, S.H., Amat, L.R., Morisseau-Leroy, N.. The HRD real-time hurricane wind analysis system. Journal of Wind Engineering and Industrial Aerodynamics 1998;77:53–64.

[7] Taflanidis, A.A., Kennedy, A.B., Westerink, J.J., Smith, J., Cheung, K.F., Hope, M., et al. Rapid assessment of wave and surge risk during landfalling hurricanes: Probabilistic approach. Journal of Waterway, Port, Coastal, and Ocean Engineering 2013;139(3):171–182.

[8] Jia, G., Taflanidis, A.A., Nadal-Caraballo, N.C., Melby, J.A., Kennedy, A.B., Smith, J.M.. Surrogate modeling for peak or time-dependent storm surge prediction over an extended coastal region using an existing database of synthetic storms. Natural Hazards 2016;81(2):909–938.

[9] Pinelli, J.P., Simiu, E., Gurley, K., Subramanian, C., Zhang, L., Cope, A., et al. Hurricane damage prediction model for residential structures. Journal of Structural Engineering 2004;130(11):1685–1691.

[10] Li, Y., Ellingwood, B.R.. Hurricane damage to residential construction in the US: Importance of uncertainty modeling in risk assessment. Engineering Structures 2006;28(7):1009–1018.

[11] Pita, G., Pinelli, J.P., Cocke, S., Gurley, K., Mitrani-Reiser, J., Weekes, J., et al. Assessment of hurricane-induced internal damage to low-rise buildings in the Florida Public Hurricane Loss Model. Journal of Wind Engineering and Industrial Aerodynamics 2012;104:76–87.

[12] Rosowsky, D.V., Cheng, N.. Reliability of light-frame roofs in high-wind regions. II: Reliability analysis. Journal of Structural Engineering 1999;125(7):734–739.

[13] Gavanski, E., Kopp, G.A., Hong, H.P.. Reliability analysis of roof sheathing panels on wood-frame houses under wind loads in Canadian cities. Canadian Journal of Civil Engineering 2014;41(8):717–727.

[14] Zhang, S., Nishijima, K., Maruyama, T.. Reliability-based modeling of typhoon induced wind vulnerability for residential buildings in Japan. Journal of Wind Engineering and Industrial Aerodynamics 2014;124:68–81.

[15] Ellingwood, B.R., Rosowsky, D.V., Li, Y., Kim, J.H.. Fragility assessment of light-frame wood construction subjected to wind and earthquake hazards. Journal of Structural Engineering 2004;130(12):1921–1930.

[16] Lee, K.H., Rosowsky, D.V.. Fragility assessment for roof sheathing failure in high wind regions. Engineering Structures 2005;27(6):857–868.

[17] Stewart, M.G., Ginger, J.D., Henderson, D.J., Ryan, P.C.. Fragility and climate impact assessment of contemporary housing roof sheeting failure due to extreme wind. Engineering Structures 2018;171:464–475.

[18] Sparks, P.R., Schiff, S., Reinhold, T.. Wind damage to envelopes of houses and consequent insurance losses. Journal of Wind Engineering and Industrial Aerodynamics 1994;53(1-2):145–155.

[19] Huang, Z., Rosowsky, D.V., Sparks, P.R.. Long-term hurricane risk assessment and expected damage to residential structures. Reliability Engineering & System Safety 2001;74(3):239–249.

[20] Stewart, M.G., Rosowsky, D.V., Huang, Z.. Hurricane risks and economic viability of strengthened construction. Natural Hazards Review 2003;4(1):12–19.

[21] Lin, N., Vanmarcke, E., Yau, S.C.. Windborne debris risk analysis-Part II. Application to structural vulnerability modeling. Wind and Structures 2010;13(2):207–220.

[22] Yau, S.C., Lin, N., Vanmarcke, E.. Hurricane damage and loss estimation using an integrated vulnerability model. Natural Hazards Review 2011;12(4):184–189.

[23] Jaimes, M.A., Nino, M.. Probabilistic wind risk assessment induced by hurricanes on economically vulnerable households in Mexico. Natural Hazards Review 2018;19(3):04018012.

[24] Grayson, J.M., Pang, W., Schiff, S.. Building envelope failure assessment framework for residential communities subjected to hurricanes. Engineering Structures 2013;51:245–258.

[25] Vickery, P.J., Lin, J., Skerlj, P.F., Twisdale Jr, L.A., Huang, K.. HAZUS-MH hurricane model methodology. I: Hurricane hazard, terrain, and wind load modeling. Natural Hazards Review 2006;7(2):82–93.

[26] Vickery, P.J., Skerlj, P.F., Lin, J., Twisdale Jr, L.A., Young, M.A., Lavelle, F.M.. HAZUS-MH hurricane model methodology. II: Damage and loss estimation. Natural Hazards Review 2006;7(2):94–103.

[27] Gurley, K., Pinelli, J.P., Subramanian, C., Cope, A.D., Zhang, L., Murphree, J., et al. Florida Public Hurricane Loss Projection Model. Engineering Team Final Report, Volume I: Exposure and Vulnerability Components of the Florida Public Hurricane Loss Projection Model. Technical Report. Tech. Rep.; International Hurricane Research Center, Florida International University, Miami, Florida, USA; 2005.

[28] Gurley, K., Pinelli, J.P., Subramanian, C., Cope, A.D., Zhang, L., Murphree, J., et al. Florida Public Hurricane Loss Projection Model. Engineering Team Final Report, Volume II: Predicting the Vulnerability of Typical Residential Buildings to Hurricane Damage, Technical Report. Tech. Rep.; International Hurricane Research Center, Florida International University, Miami, Florida, USA; 2005.

[29] Rosowsky, D.V., Ellingwood, B.R.. Performance-based engineering of wood frame housing: Fragility analysis methodology. Journal of Structural Engineering 2002;128(1):32–38.

[30] van de Lindt, J.W., Dao, T.N.. Performance-based wind engineering for wood-frame buildings. Journal of Structural Engineering 2009;135(2):169–177.

[31] Dao, T.N., van de Lindt, J.W., Prevatt, D.O., Gupta, R.. Probabilistic procedure for wood-frame roof sheathing panel debris impact to windows in hurricanes. Engineering Structures 2012;35:178–187.

[32] Barbato, M., Petrini, F., Unnikrishnan, V.U., Ciampoli, M.. Performance-based hurricane engineering (PBHE) framework. Structural Safety 2013;45:24–35.

[33] Smith, M.A., Caracoglia, L.. A Monte Carlo based method for the dynamic "fragility analysis" of tall buildings under turbulent wind loading. Engineering Structures 2011;33(2):410–420.

[34] Petrini, F., Ciampoli, M.. Performance-based wind design of tall buildings. Structure and Infrastructure Engineering 2012;8(10):954–966.

[35] Chuang, W.C., Spence, S.M.J.. A performance-based design framework for the integrated collapse and non-collapse assessment of wind excited buildings. Engineering Structures 2017;150:746–758.

[36] Cui, W., Caracoglia, L.. A unified framework for performance-based wind engineering of tall buildings in hurricane-prone regions based on lifetime intervention-cost estimation. Structural Safety 2018;73:75–86.

[37] Zheng, X.W., Li, H.N., Li, C.. Damage probability analysis of a high-rise building against wind excitation with recorded field data and direction effect. Journal of Wind Engineering and Industrial Aerodynamics 2019;184:10–22.

[38] Cui, W., Caracoglia, L.. Performance-based wind engineering of tall buildings examining life-cycle downtime and multisource wind damage. Journal of Structural Engineering 2020;146(1):04019179.

[39] Ouyang, Z., Spence, S.M.J.. A performance-based damage estimation framework for the building envelope of wind-excited engineered structures. Journal of Wind Engineering and Industrial Aerodynamics 2019;186:139–154.

[40] Ouyang, Z., Spence, S.M.J.. Performance-based wind-induced structural and envelope damage assessment of engineered buildings through nonlinear dynamic analysis. Journal of Wind Engineering and Industrial Aerodynamics 2021;208(1):104452.

[41] Ciampoli, M., Petrini, F., Augusti, G.. Performance-based wind engineering: towards a general procedure. Structural Safety 2011;33(6):367–378.

[42] Kameshwar, S., Padgett, J.E.. Multi-hazard risk assessment of highway bridges subjected to earthquake and hurricane hazards. Engineering Structures 2014;78:154–166.

[43] Spence, S.M.J., Arunachalam, S.. Performance-based wind engineering: Background and state of the art. Frontiers in Built Environment 2022;26:830207.

[44] Ouyang, Z., Spence, S.M.J.. A performance-based wind engineering framework for envelope systems of engineered buildings subject to directional wind and rain hazards. Journal of Structural Engineering 2020;146(5):04020049.

[45] Ouyang, Z., Spence, S.M.J.. Performance-based wind-induced structural and envelope damage assessment of engineered buildings through nonlinear dynamic analysis. Journal of Wind Engineering and Industrial Aerodynamics 2021;208:104452.

[46] Box, G.E.P., Wilson, K.B.. On the experimental attainment of optimum conditions. Journal of the Royal Statistical Society: Series B (Methodological) 1951;13(1):1–38.

[47] Whitney, A.W.. A direct method of nonparametric measurement selection. IEEE Transactions on Computers 1971;100(9):1100–1103.

[48] Friedman, J., Hastie, T., Tibshirani, R.. The elements of statistical learning. Springer, New York, USA; 2001.

[49] Friedman, J.H.. Multivariate adaptive regression splines. The Annals of Statistics 1991;19(1):1–67.

[50] Ghosh, J., Padgett, J.E., Dueñas-Osorio, L.. Surrogate modeling and failure surface visualization for efficient seismic vulnerability assessment of highway bridges. Probabilistic Engineering Mechanics 2013;34:189–199.

[51] Segura, R., Padgett, J.E., Paultre, P.. Metamodel-based seismic fragility analysis of concrete gravity dams. Journal of Structural Engineering 2020;146(7):04020121.

[52] Jekabsons, G., Zhang, Y.. Adaptive basis function construction: An approach for adaptive building of sparse polynomial regression models. Machine Learning 2010;1(10):127–155.

[53] Breitkopf, P., Naceur, H., Rassineux, A., Villon, P.. Moving least squares response surface approximation: Formulation and metal forming applications. Computers & Structures 2005;83(17-18):1411–1428.

[54] Taflanidis, A.A., Jia, G., Kennedy, A.B., Smith, J.M.. Implementation/optimization of moving least squares response surfaces for approximation of hurricane/storm surge and wave responses. Natural Hazards 2013;66(2):955–983.

[55] Kim, S.W., Melby, J.A., Nadal-Caraballo, N.C., Ratcliff, J.. A time-dependent surrogate model for storm surge prediction based on an artificial neural network using high-fidelity synthetic hurricane modeling. Natural Hazards 2015;76(1):565–585.

[56] Le, V., Caracoglia, L.. A neural network surrogate model for the performance assessment of a vertical structure subjected to non-stationary, tornadic wind loads. Computers & Structures 2020;231:106208.

[57] Hardy, R.L.. Multiquadric equations of topography and other irregular surfaces. Journal of Geophysical Research 1971;76(8):1905–1915.

[58] Sacks, J., Welch, W.J., Mitchell, T.J., Wynn, H.P.. Design and analysis of computer experiments. Statistical Science 1989;4(4):409–423.

[59] Jakobsen, F., Madsen, H.. Comparison and further development of parametric tropical cyclone models for storm surge modelling. Journal of Wind Engineering and Industrial Aerodynamics 2004;92(5):375–391.

[60] Ouyang, Z., Spence, S.M.J.. A performance-based wind engineering framework for engineered building systems subject to hurricanes. Frontiers in Built Environment 2021;7:720764.

[61] National Hurricane Center (NHC). National hurricane center (NHC). 2021. URL: https://www.nhc.noaa.gov/.

[62] National Hurricane Center (NHC). National hurricane center forecast verification. 2021. URL: https://www.nhc.noaa.gov/verification/verify7.shtml.

[63] Shapiro, L.J.. The asymmetric boundary layer flow under a translating hurricane. Journal of Atmospheric Sciences 1983;40(8):1984–1998.

[64] Hubbert, G.D., Holland, G.J., Leslie, L.M., Manton, M.J.. A real-time system for forecasting tropical cyclone storm surges. Weather and Forecasting 1991;6(1):86–97.

[65] Vickery, P.J., Twisdale, L.A.. Wind-field and filling models for hurricane wind-speed predictions. Journal of Structural Engineering 1995;121(11):1700–1709.

[66] Powell, M.D.. Evaluations of diagnostic marine boundary-layer models applied to hurricanes. Monthly Weather Review 1980;108(6):757–766.

[67] Simiu, E., Vickery, P., Kareem, A.. Relation between Saffir–Simpson hurricane scale wind speeds and peak 3-s gust speeds over open terrain. Journal of Structural Engineering 2007;133(7):1043–1045.

[68] Simiu, E., Scanlan, R.H.. Wind effects on structures : an introduction to wind engineering. Wiley, New York; 1986.

[69] Chen, X., Kareem, A.. Proper orthogonal decomposition-based modeling, analysis, and simulation of dynamic wind load effects on structures. Journal of Engineering Mechanics 2005;131(4):325–339.

[70] Gioffrè, M., Gusella, V., Grigoriu, M.. Non-Gaussian wind pressure on prismatic buildings. I: Stochastic field. Journal of Structural Engineering 2001;127(9):981–989.

[71] Zhao, H., Grigoriu, M., Gurley, K.R.. Translation processes for wind pressures on low-rise buildings. Journal of Wind Engineering and Industrial Aerodynamics 2019;184:405–416.

[72] Vickery, B.J., Bloxham, C.. Internal pressure dynamics with a dominant opening. Journal of Wind Engineering and Industrial Aerodynamics 1992;41(1-3):193–204.

[73] Guha, T.K., Sharma, R.N., Richards, P.J.. Internal pressure dynamics of a leaky building with a dominant opening. Journal of Wind Engineering and Industrial Aerodynamics 2011;99(11):1151–1161.

[74] Beason, W.L., Morgan, J.R.. Glass failure prediction model. Journal of Structural Engineering 1984;110(2):197–212.

[75] American Society for Testing and Materials. Standard practice for determining load resistance of glass in buildings (ASTM E1300). Standard; American Society for Testing and Materials; ASTM International, West Conshohocken, PA, USA; 2016.

[76] Rasmussen, C.E.. Gaussian processes in machine learning. In: Bousquet, O., von Luxburg, U., Rätsch, G., editors. Advanced Lectures on Machine Learning: Machine Learning Summer Schools 2003, Tübingen, Germany. Berlin, Heidelberg, Germany: Springer; 2004, p. 63–71.

[77] Forrester, A., Sobester, A., Keane, A.. Engineering design via surrogate modelling: A practical guide. John Wiley & Sons, Hoboken, NJ, USA; 2008.

[78] Jia, G., Taflanidis, A.A.. Kriging metamodeling for approximation of high-dimensional wave and surge responses in real-time storm/hurricane risk assessment. Computer Methods in Applied Mechanics and Engineering 2013;261:24–38.

[79] Lophaven, S.N., Nielsen, H.B., Søndergaard, J.. Aspects of the Matlab toolbox DACE. Tech. Rep.; Technical University of Denmark, Copenhagen, Denmark; 2002.

[80] Tokyo Polytechnic University. Tokyo polytechnic university wind pressure database. 2008. URL: `http://www.wind.arch.t-kougei.ac.jp/system/eng/contents/code/tpu`.

[81] Federal Emergency Management Agency. Seismic performance assessment of buildings (Volume 1-Methodology, FEMA P58-1). Standard; Federal Emergency Management Agency; Washington, USA; 2012.

[82] Behr, R.A., Karson, M.J., Minor, J.E.. Reliability analysis of window glass failure pressure data. Structural Safety 1991;11(1):43–58.

[83] Stewart, S.R.. National hurricane center tropical cyclone report: Hurricane Matthew (AL142016): 28 September–9 October 2016. Tech. Rep.; National Hurricane Center (NHC); 2017.

[84] Cangialosi, J.P., Latto, A.S., Berg, R.. National hurricane center tropical cyclone report: Hurricane Irma (AL112017): 30 August–12 September 2017. Tech. Rep.; National Hurricane Center (NHC); 2018.

[85] Avila, L.A., Stewart, S.R., Berg, R., Hagen, A.B.. National hurricane center tropical cyclone report: Hurricane Dorian (AL052019): 24 August–7 September 2019. Tech. Rep.; National Hurricane Center (NHC); 2020.

[86] Vickery, P.J., Twisdale, L.A.. Prediction of hurricane wind speeds in the United States. Journal of Structural Engineering 1995;121(11):1691–1699.

[87] Landsea, C.W., Franklin, J.L.. Atlantic hurricane database uncertainty and presentation of a new database format. Monthly Weather Review 2013;141(10):3576–3592.

[88] Vickery, P.J., Skerlj, P., Steckley, A., Twisdale, L.. Hurricane wind field model for use in hurricane simulations. Journal of Structural Engineering 2000;126(10):1203–1221.